



Delft University of Technology

Aerodynamic Performance of an Aircraft with Aft-Fuselage Boundary-Layer-Ingestion Propulsion

della Corte, B.; van Sluis, M.; Gangoli Rao, A.; Veldhuis, L.L.M.

DOI

[10.2514/1.C036596](https://doi.org/10.2514/1.C036596)

Publication date

2022

Document Version

Accepted author manuscript

Published in

Journal of Aircraft: devoted to aeronautical science and technology

Citation (APA)

della Corte, B., van Sluis, M., Gangoli Rao, A., & Veldhuis, L. L. M. (2022). Aerodynamic Performance of an Aircraft with Aft-Fuselage Boundary-Layer-Ingestion Propulsion. *Journal of Aircraft: devoted to aeronautical science and technology*, 59(4), 1054-1070. <https://doi.org/10.2514/1.C036596>

Important note

To cite this publication, please use the final published version (if applicable).

Please check the document version above.

Copyright

Other than for strictly personal use, it is not permitted to download, forward or distribute the text or part of it, without the consent of the author(s) and/or copyright holder(s), unless the work is under an open content license such as Creative Commons.

Takedown policy

Please contact us and provide details if you believe this document breaches copyrights.

We will remove access to the work immediately and investigate your claim.



Aerodynamic Performance of an Aircraft with Aft-Fuselage Boundary-Layer-Ingestion Propulsion

Biagio Della Corte,^{*} Martijn van Sluis,[†] Arvind Gangoli Rao,[‡] and Leo L. M. Veldhuis[§]

Delft University of Technology, Delft, The Netherlands

<https://doi.org/10.2514/1.C036596>

Boundary-layer ingestion (BLI) is a propulsor-airframe integration technology that promises substantial fuel consumption benefits for future civil aircraft. This paper discusses an experimental study, conducted within the European Union-funded Horizon 2020 CENTRELINe project, on the aerodynamic performance of an aircraft with a BLI propulsor integrated at the aft-fuselage section (known as the Propulsive Fuselage Concept). The low-speed wind-tunnel experiments were carried out at Reynolds and Mach numbers of 460,000 and 0.12, whereas the Reynolds and Mach numbers are 40,000,000 and 0.82 at full-flight scale. Aerodynamic loads measurements show that the BLI propulsor affects the longitudinal and lateral-directional equilibrium of the aircraft in off-cruise conditions. Moreover, velocity and total pressure measurements characterize the flowfield around the BLI propulsor in cruise and off-cruise conditions. The analysis of the momentum and power fluxes in the flowfield shows that, while around 20% of the total aircraft drag is due to the fuselage body, only less than 5% of the total aircraft drag power is dissipated in the fuselage wake. Furthermore, the BLI propulsor recovers around 50% the axial kinetic energy flux in the fuselage boundary layer (the so-called wake-filling effect), suggesting an increased propulsive efficiency.

Nomenclature

C_D	= drag coefficient, $D/q_\infty S$	L_b	= fuselage body length, m
C_L	= lift coefficient, $L/q_\infty S$	\mathcal{M}	= pitch moment, $N \cdot m$
C_L	= roll moment coefficient, $\mathcal{L}/q_\infty S c$	\mathcal{N}	= yaw moment, $N \cdot m$
C_M	= pitch moment coefficient, $\mathcal{M}/q_\infty S c$	R_b	= fuselage body radius, m
C_N	= yaw moment coefficient, $\mathcal{N}/q_\infty S c$	$Re_{\bar{c}}$	= mean-chord-based Reynolds number, equal to $\rho_\infty V_\infty c / \mu_\infty$
C_{p_t}	= total pressure coefficient, $(p_t - p_{t\infty})/q_\infty$	p	= pressure, Pa
C_Y	= lateral force coefficient, $Y/q_\infty S$	p_t	= total pressure, Pa
\bar{c}	= wing mean aerodynamic chord, m	q	= dynamic pressure, Pa
c_f	= fan midspan chord, m	S	= wing planform area, m^2
D	= drag force, N	U_{tip}	= fan tip speed, m/s
D_f	= fan diameter, m	u, v, w	= Cartesian velocity components, m/s
D_0	= reference drag force, N	u, v_r, v_t	= cylindrical velocity components, m/s
$d\dot{E}_a$	= axial kinetic energy flux density, W/m^2	V	= velocity magnitude, m/s
$d\dot{E}_p$	= pressure work density, W/m^2	x, r, ϕ	= body reference system
$d\dot{E}_v$	= transverse kinetic energy flux density, W/m^2	x, y, z	= Cartesian coordinates
dF_a	= axial momentum flux density, equal to $-dF_x$, N/m^2	x_B, y_B, z_B	= body reference system
dF_x	= axial momentum flux density, N/m^2	Y	= side force, N
\dot{E}_a	= axial kinetic energy flow rate, W	α	= angle of attack, deg
\dot{E}_p	= pressure work rate, W	β	= angle of sideslip, deg
\dot{E}_v	= transverse kinetic energy flow rate, W	Γ	= circulation, m^2/s
F_a	= axial momentum flow rate, equal to $-F_x$, N	ζ	= radial angle, deg
F_i	= i th component of boundary-layer ingestion propulsor inflow	θ	= swirl angle, deg
F_x	= axial momentum flow rate, N	μ	= dynamic viscosity, $Pa \cdot s$
L	= lift force, N	ρ	= density, kg/m^3
\mathcal{L}	= roll moment, $N \cdot m$	ϕ	= azimuthal angular position, deg
		Ω	= fan angular velocity, rad/s
		ω	= vorticity, s^{-1}

Subscript

∞	= freestream conditions
----------	-------------------------

I. Introduction

Presented as Paper 2021-2467 at the AIAA AVIATION 2021 FORUM, Virtual Event, August 2-6, 2021; received 30 July 2021; revision received 20 December 2021; accepted for publication 19 March 2022; published online 26 April 2022. Copyright © 2022 by The Authors. Published by the American Institute of Aeronautics and Astronautics, Inc., with permission. All requests for copying and permission to reprint should be submitted to CCC at www.copyright.com; employ the eISSN 1533-3868 to initiate your request. See also AIAA Rights and Permissions www.aiaa.org/randp.

*Ph.D. Candidate, Flight Performance and Propulsion Group, Faculty of Aerospace Engineering; B.DellaCorte@tudelft.nl.

†Ph.D. Candidate, Flight Performance and Propulsion Group, Faculty of Aerospace Engineering.

‡Associate Professor, Flight Performance and Propulsion Group, Faculty of Aerospace Engineering; A.GangoliRao@tudelft.nl.

§Full Professor, Section Head, Flight Performance and Propulsion Group, Faculty of Aerospace Engineering.

is reduced (the so-called wake-filling effect of BLI). Second, the kinetic energy in the boundary layer and ingested by the propulsor results in a reduction of the required mechanical power (see Refs. [4–6]).

In the last decade, BLI has been investigated in numerous unconventional aircraft concepts with an estimated power benefit over a conventional architecture ranging from 5 to 10% (see, e.g., Refs. [7–11]). One of the most promising configuration is the Propulsive Fuselage Concept (PFC), a tube-and-wing aircraft in which an aft-fuselage mounted BLI propulsor ingests the fuselage boundary layer [12–14]. A sketch of the PFC is presented in Fig. 1. The PFC has various advantages over other BLI configurations. First, the momentum deficit share which can be ingested with a single propulsor is maximized [15]. Moreover, the inlet distortions for the BLI propulsor are minimized, because the fuselage boundary layer can ideally be axisymmetric, resulting in minimum propulsor losses [16]. Finally, the airframe design changes are minimized because the PFC implements BLI on an otherwise conventional architecture. Because of these reasons, BLI propulsion applied to a fuselage body has been extensively studied in recent years. Experimental work has investigated the physical mechanisms responsible for BLI benefits and quantified the power savings [17,18]. Moreover, numerical studies have demonstrated the effects of the propulsor–airframe interactions on the resulting aeropropulsive performance both in axisymmetric and in three-dimensional flow conditions [19,20]. One drawback of these interactions is an increase of the fuselage body drag induced by the propulsor pressure and velocity fields. The drag penalty, almost entirely due to an increase in the pressure drag term, was quantified through numerical analysis at around 6% for a generic axisymmetric body with a BLI propulsor [5].

The CENTRELINE project, funded by the European Union within the Horizon 2020 framework, proposed a turboelectric PFC for a long-range wide-body commercial aviation aircraft [14]. The concept, sketched in Fig. 1, features an aft-fuselage-mounted shrouded fan driven by an electric motor powered by the under-the-wing turbofans. During cruise, the BLI propulsor provides around 25% of the total propulsive power to maximize the system-level benefit [21]. Both the fuselage and the fan stage were designed assuming axisymmetric conditions. The axisymmetric fuselage and shroud contours were optimized to maximize the propulsive force for a given shaft power [31]. At the same time, the fan stage design minimized the losses in efficiency induced by the inlet distortions due to the fuselage boundary layer [16]. A previous related work has experimentally investigated the aerodynamic performance of an axisymmetric propulsive fuselage representative of the CENTRELINE concept [22]. The study analyzed the aerodynamic interactions between the fuselage airframe and the BLI propulsor in axial inflow conditions. The work highlighted that the propulsor has a strong effect on the fuselage boundary layer. Because of the suction imposed to the fluid, higher velocity is found in the near-wall region of the boundary layer upstream of the propulsor, and high-momentum flow is drawn toward the fuselage wall, which reduces the local boundary-layer thickness.

However, in a more realistic scenario, the flow around the fuselage aft section is not expected to be axisymmetric, as it will result from the influences of different elements. In particular, the fuselage-mounted shrouded fan will be affected by other aerodynamic surfaces and elements of the aircraft, namely, the wing and vertical tail plane. These elements will introduce total pressure and velocity distortions at the fan inlet due to viscous dissipation (i.e., boundary layers and wakes) or circulation (i.e., lift) which are a function of the flight conditions. These distortions can have an impact on propulsive efficiency, stall margin, and aeromechanic and aeroacoustic performance of the fan (see, e.g., Refs. [23–27]). Moreover, the aerodynamic interaction between the BLI propulsor and the aircraft airframe can have an effect on the overall system aerodynamic performance and influence the local flowfield around the fuselage aft-cone section. A schematic of the main flow distortions and aerodynamic interaction expected in the propulsive fuselage is presented in Fig. 1.

To tailor the PFC design to minimize installation penalties and hence maximize the aeropropulsive efficiency, the main flow phenomena need to be investigated. This paper discusses an experimental analysis of an aircraft model representative of the CENTRELINE Propulsive Fuselage Concept. The model featured a shrouded BLI propulsor integrated at the aft fuselage section. The goal of the low-speed wind-tunnel experiments was twofold. First was to assess the effect of the BLI fan on the aircraft forces in various flight conditions. Second was to characterize the aerodynamic flow around the BLI propulsor in on- and off-design conditions.

II. Methods

Low-speed wind-tunnel tests were performed on a subscaled aircraft model equipped with a fuselage-mounted BLI shrouded fan. As a consequence of the scaling limitations, the Reynolds and Mach numbers characterizing the flow at the laboratory scale were lower than the expected values in typical high-subsonic cruise conditions. In particular, the wind-tunnel experiments were conducted at a wing-mean-chord-based Reynolds number Re_c of 460,000 and a Mach number M of 0.12. As a reference, in full-scale cruise conditions, Re_c and M would be 40,000,000 and 0.82, respectively. The Reynolds and Mach numbers scaling affects important aspects of the PFC aerodynamics, for example, the fuselage boundary layer, the BLI fan aerodynamics and efficiency, and the fuselage–vertical tail plane (VTP) junction flow. Because of the lower Reynolds number obtained during the experiments, delayed turbulent transition and relatively larger boundary-layer thicknesses were expected compared to the full-scale flight conditions. To mitigate these effects, the transition locations were imposed on all the fixed aerodynamic surfaces (fuselage, wing, vertical tail, and shroud) through tripping elements. Moreover, the BLI propulsor model was sized accordingly to the fuselage boundary-layer thickness to maintain the same scaling relative to the boundary-layer thickness as found in full-scale aircraft. Compressibility effects could not be simulated in the low-speed wind tunnel used. Compressibility plays a major role in the aerodynamics of lifting surfaces (i.e., wings). However, the consequences of the low

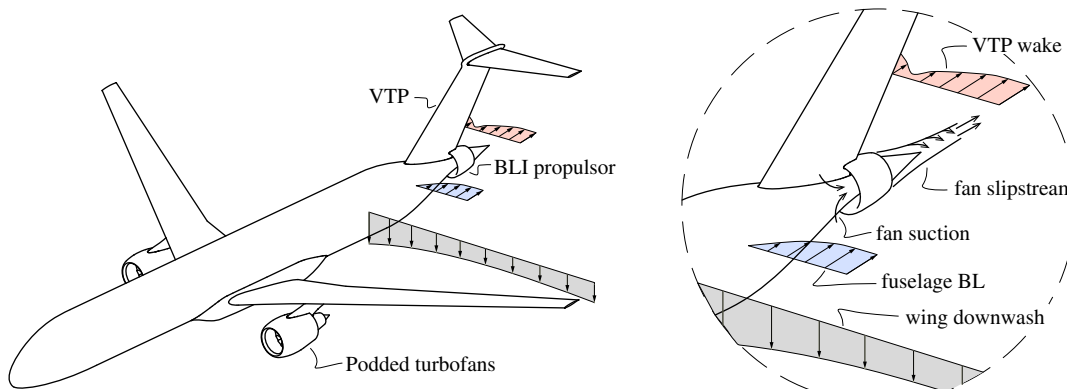


Fig. 1 Schematic of the CENTRELINE Propulsive Fuselage Concept. Based on Refs. [14,16].

Mach number are not expected to have a strong influence on the flow around the fuselage body because the critical Mach number of axisymmetric bodies is higher than the typical cruise Mach number (see, for example, Refs. [28–30]). As a consequence of the scaling limitations, quantitative results obtained at low speed are not directly scalable to full-scale conditions. However, qualitative comparison with numerical simulations at the full-scale regime performed within the CENTRELINe project (see Refs. [14] and [31]) showed that the key aerodynamic phenomena are qualitatively similar to the findings of the low-speed wind-tunnel experiments.

Furthermore, the aircraft model tested was representative of the CENTRELINe Propulsive Fuselage Concept design. However, except for some aspects (e.g., the contour of the fuselage aft cone), the model design was simplified to avoid configuration-specific design choices being able to affect some of the findings of this study. In particular, the aircraft model was not equipped with an horizontal tail, as no significant aerodynamic interactions were expected between the horizontal tail plane and the BLI propulsor. Similarly, the aircraft trim condition was not accounted for in this study, as it was not expected to significantly alter the flowfield around the fuselage aft cone and the BLI propulsor.

Finally, because the focus of the experiment was to study the aerodynamic interaction between the aircraft and the installed BLI propulsor, and not to quantify the aircraft performance, wind-tunnel corrections were not applied, and the results are based on uncorrected data.

A. Wind-Tunnel Facility and Setup

The wind-tunnel experiments were carried out at the Low Turbulence Tunnel (LTT) of Delft University of Technology. The LTT is a closed-loop, closed test-section atmospheric wind tunnel. The test section features an octagonal cross-section with a width of 1.80 m and height of 1.25 m. The maximum test speed that can be reached is 120 m/s with a turbulence intensity below 0.1%.

The test setup consisted of an aircraft model representative of the CENTRELINe PFC. Photographs of the model installed in the test section are shown in Fig. 2, and the main model dimensions are reported in Fig. 3. The reference systems and conventions used in the current study are reported in Fig. 4.

The aircraft model was mounted to an external six-components balance through a three-point attachment system. The support structures were hinged to the two wings and to the aft-fuselage section. The model could rotate around the wing-support hinge axis to simulate an angle of attack α , which was controlled by vertically sliding the aft-fuselage support. In addition, the model could rotate around the vertical axis to simulate an angle of sideslip β . The support struts rotated with the model and with a turntable embedded in the test-section wall.

The fuselage consisted of an axisymmetric body with a maximum radius R_b of 70 mm and a total length L_b of 1564 mm. The fuselage aft-cone section shape was adapted from the propulsive aft cone of the

CENTRELINe PFC aircraft. Moreover, the fuselage aft-cone section was modular, allowing the testing of different configurations which are described in more detail in Sec. II.C.1.

The fuselage aft-cone section was equipped with a BLI shrouded propulsor, of which technical views and details are shown in Fig. 5. The fan featured 12 blades with a diameter D_f of 75 mm, a hub-to-tip-radii ratio of 0.41, and a midspan blade chord c_f of 22 mm. The fan was driven by a three-phase brushless electric motor, and its rotational speed Ω was measured through a US Digital® optical encoder mounted on the motor shaft.

Because the fuselage boundary layer is expected to be relatively larger at the test scale when compared to the flight scale (due to the lower Reynolds number), the propulsor size was not scaled geometrically from the full scale to the wind-tunnel scale. Aerodynamic and aero-propulsive similarity between the wind-tunnel model and the full-scale aircraft were obtained by 1) scaling the propulsor size such that the same ratio between the fan diameter and the fuselage momentum thickness at the fan location is achieved and 2) optimizing the fan blades at the same operating conditions defined by the flow coefficient and load coefficient. The shroud geometry was also adapted from the full-scale CENTRELINe configuration to allow a tip gap of 0.75 mm, approximately corresponding to 1% of D_f . The shroud was equipped with five inlet and outlet vanes. The inlet vanes featured a NACA 0015 airfoil section with a rectangular planform. These vanes supported the shroud and were not optimized to deswirl the flow. A more detailed discussion of the procedures and tools used in the fan design can be found in Ref. [32].

The unswept low wing (mean chord \bar{c} of 165 mm and planform area S of 0.216 m²) featured a cambered airfoil, an aspect ratio of 8.46, a taper ratio of 0.4, and a linear washout of 2 deg. The VTP featured a symmetric NACA 0012 airfoil, a taper ratio of 0.3, and a leading edge sweep angle of 30 deg.

Boundary-layer transition was forced on all the surfaces through 2.5 mm wide strips of 140 μm carborundum particles. The strips were placed on the fuselage, shroud, vertical tail, and wing suction side at 5% of their respective lengths and at 10% of the wing chord on the wing pressure side. Occurrence of transition was checked with microphone inspections of the boundary layer at all the operating conditions that were tested during the experiments.

B. Measurement Techniques

1. Force and Moments Measurements

The aerodynamic forces and moments acting on the model were measured through the external six-components balance, to which the model was connected through the three supports. Only the model and the fuselage strut were sensed by the balance because the wing struts were almost entirely covered by fairings bolted directly to the wind-tunnel wall (see Fig. 2). The balance readings were acquired for 15 s and time averaged to filter the

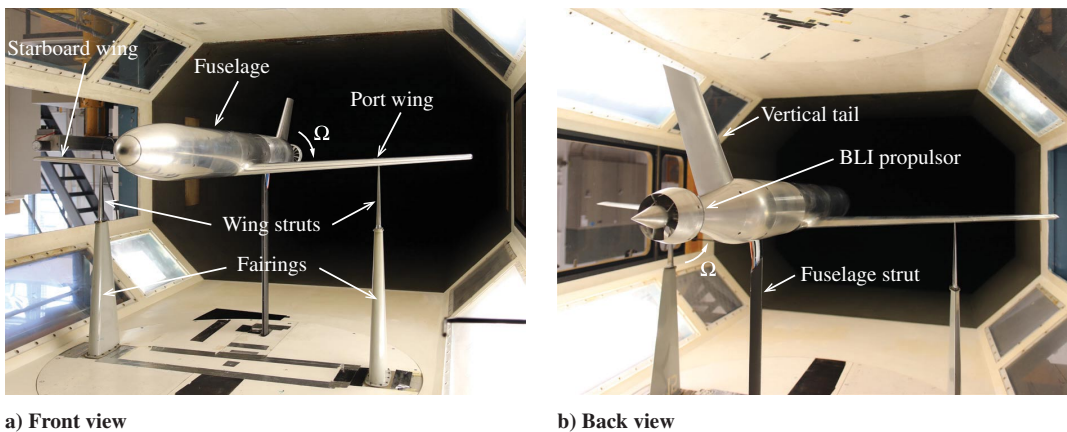


Fig. 2 Photographs of the wind-tunnel setup assembled in the test section of the Low Turbulence Tunnel of Delft University of Technology.

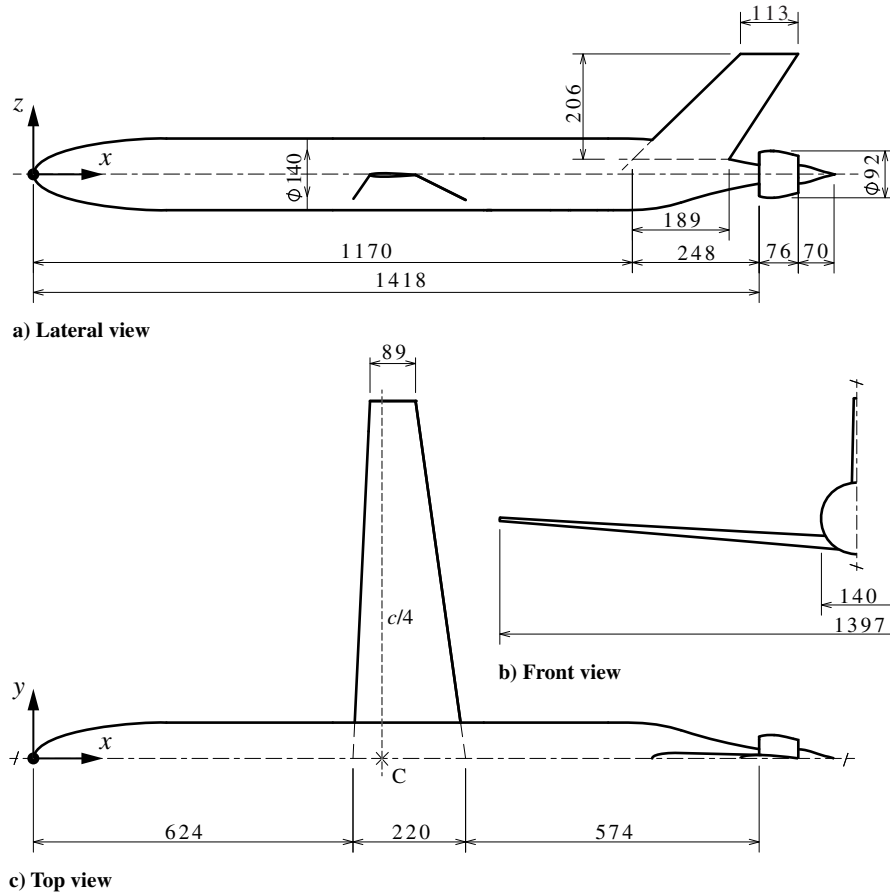
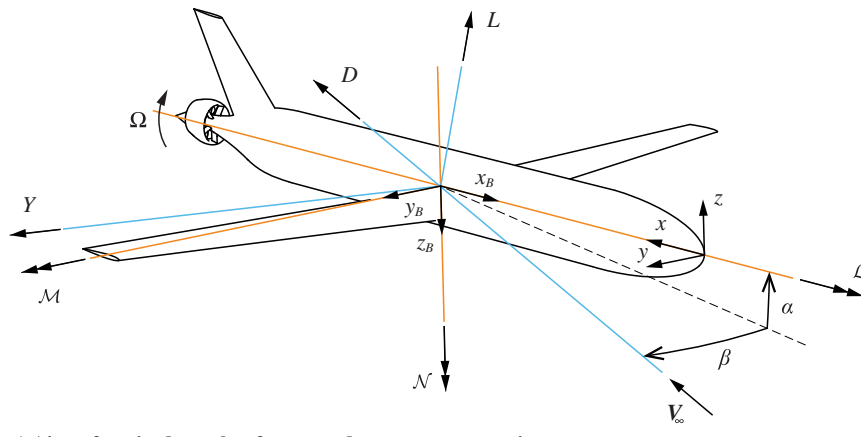
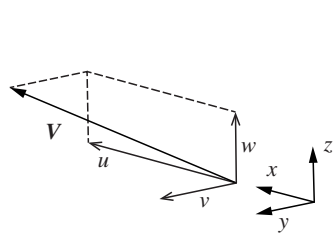


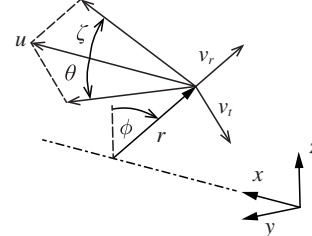
Fig. 3 Technical views of the wind-tunnel model (dimensions in millimeters).



a) Aircraft attitude angles, forces, and moments conventions



b) Cartesian velocity components



c) Cylindrical velocity components

Fig. 4 Conventions and definitions used for the aircraft forces and moments and velocity components.

fluctuations due to turbulence, vibrations, and other external factors. The nondimensional force coefficients were defined using the freestream dynamic pressure q_∞ and the wing planform area S as reference values. The uncertainty of the balance measurements was

estimated from the deviation of repeated measurements. Table 1 reports the maximum absolute deviations from the mean measured for each force and moment coefficient for two different incidence settings.

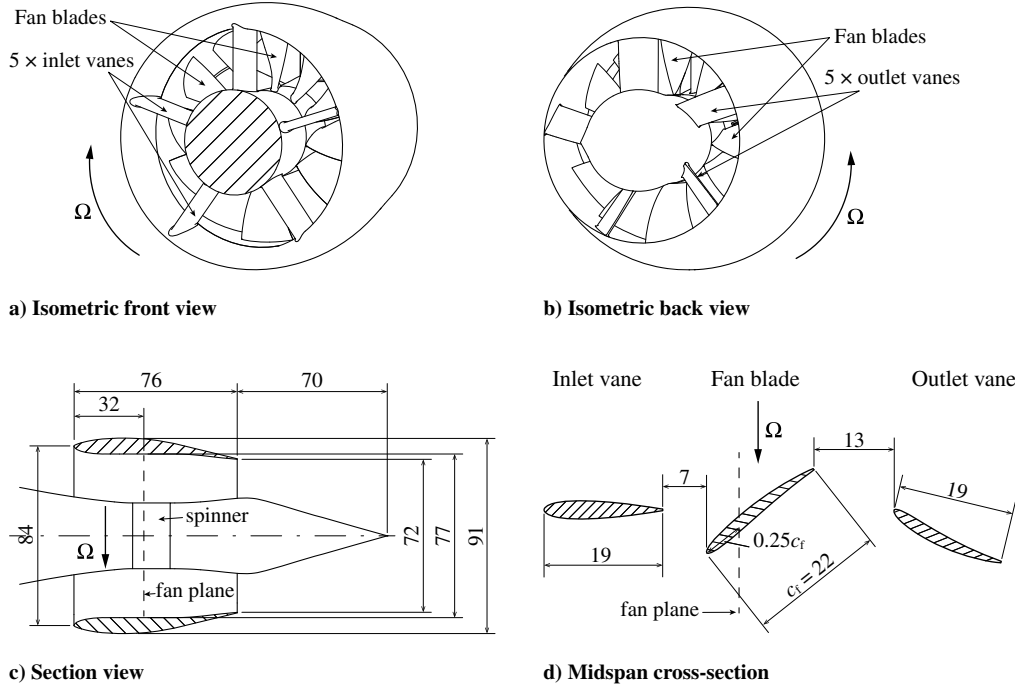


Fig. 5 Details of the shrouded BLI propulsor equipping the wind-tunnel model (dimensions in millimeters).

Table 1 Uncertainty values on the forces and moments coefficient measured through the external six-components balance

Incidence	C_L	C_D	C_Y	C_M	C_N	C_L
$\alpha = 0$ deg	0.0005	0.0002	0.0004	0.0009	0.0007	0.0009
$\beta = 0$ deg						
$\alpha = 12$ deg	0.0025	0.0004	0.0006	0.0010	0.0007	0.0012
$\beta = 0$ deg						

2. Total Pressure Measurements

The total pressure distribution upstream of the fan inlet was measured with a L-shaped pitot probe with an outer diameter of 0.6 mm. The probe was traversed in planes perpendicular to the freestream velocity direction with a variable spacing to account for the local gradients. The measurements were carried out both at cruise conditions ($\alpha = \beta = 0$ deg) and for nonzero angles of attack or sideslip. At cruise conditions ($\alpha = \beta = 0$ deg), the total pressure distribution was measured also downstream of the fan outlet plane. For the cases under sideslip, measurements at positive and negative β were combined to obtain the complete flowfield. Figure 6 shows the position and orientations of the survey planes used for the different cases.

At each probe position, after a settling time of 2 s, the pressure data were recorded through an electronic pressure scanner for a period of 5 s and averaged over this period. Simultaneously, the freestream static and total pressures were measured with a pitot static probe mounted at the inlet of the test section and acquired through the same pressure scanner. In this way, possible fluctuations in the freestream conditions due to temperature or velocity drifts could be accounted for. The raw total pressure measurements were used to define the nondimensional total pressure coefficient: $C_{p_t} = (p_t - p_{t\infty})/q_\infty$.

3. Stereoscopic Particle Image Velocimetry

Stereoscopic particle image velocimetry (PIV) was employed to quantify the three velocity components in survey planes perpendicular to the freestream around the BLI propulsor for the cruise conditions ($\alpha = \beta = 0$ deg). The PIV planes coincided with the total pressure measurements planes which are sketched in Fig. 6a. The PIV system (laser, optics, and cameras) were mounted on an electronic traversing

system, which was used to translate the measurement plane. Two LaVision[®] Imager sCMOS cameras (16-bit 2560 × 2160 pixels) were used to record the particle images. The cameras were equipped with Nikon[®] AF Micro Nikkor 105 mm 1:2.8 D lenses set at an aperture of f/11 and mounted on LaVision Scheimpflug adapter rings. A Quantel[®] Evergreen (double-pulse neodymium-doped yttrium aluminum garnet (Nd:YAG), 200 mJ) laser and coated laser optics were used to generate the laser sheets with a thickness of around 2 mm. A Safex[®] Twin Fog smoke generator was used to seed the flow with Safex Inside Nebelfluid. The seeding was injected downstream of the test section and spread uniformly in the entire flowfield within the wind-tunnel circuit. The image acquisition was controlled via a LaVision Programmable Time Unit PTU X. The image pairs were recorded at a frequency of around 10 Hz and with a pulse delay of around 30 μ s. For each case, a set of 500 phase-uncorrelated image pairs was acquired. The processing of the raw images was carried out in LaVision Davis 8.4 using an iterative multi-pass correlation algorithm with a decreasing interrogation window size (from 96 × 96 pixels for the first pass to 32 × 32 pixels for the last pass, with an overlap factor of 50%), leading to a final vector field resolution of 0.25 mm. The uncertainty of the resulting velocity field was estimated directly at the correlation phase, using a statistical analysis of the correlation function implemented in LaVision Davis 8.4 (see Ref. [33]). The uncertainty value resulted in around $0.010V_\infty$ for the velocity components and around $0.015V_\infty$ for the velocity magnitude.

C. Investigated Cases

1. Geometric Configuration

The modularity of the model allowed for the testing of four different geometric configurations, which are sketched in Fig. 7. In particular, the two main configurations were a) the bare fuselage (BF), obtained by removing the BLI propulsor, and b) the powered fuselage (PF), obtained by equipping the fuselage with the shrouded fan. For each of these configurations, the vertical tail plane could be installed (VTP on) and disassembled (VTP off).

2. Flow and Operating Conditions

All the measurements were taken at a freestream velocity V_∞ of 40 m/s, corresponding to a freestream Reynolds number based on the wing mean chord $Re_{\bar{c}}$ of around 460,000 and a Mach number of 0.12. At this freestream velocity, the freestream turbulence level is lower than 0.03% of V_∞ [34]. The angle of attack α was varied

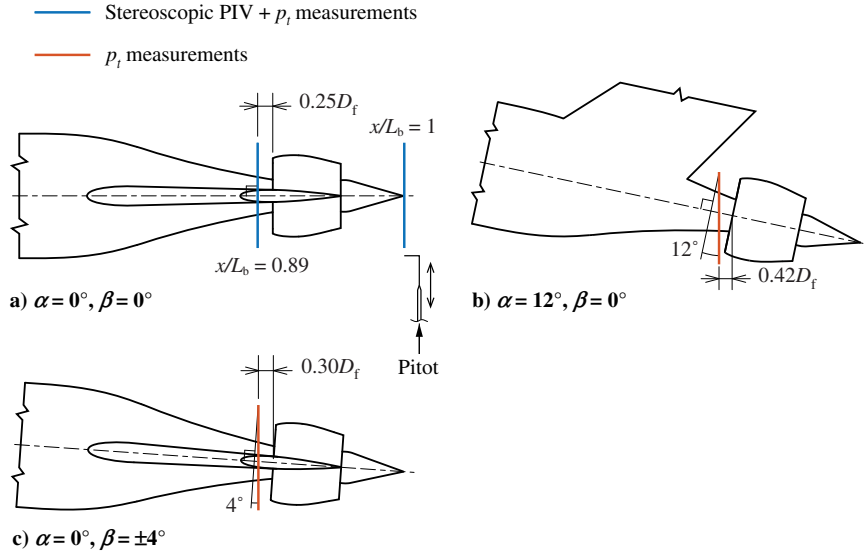


Fig. 6 Location and orientation of the total pressure and stereoscopic PIV measurements planes.

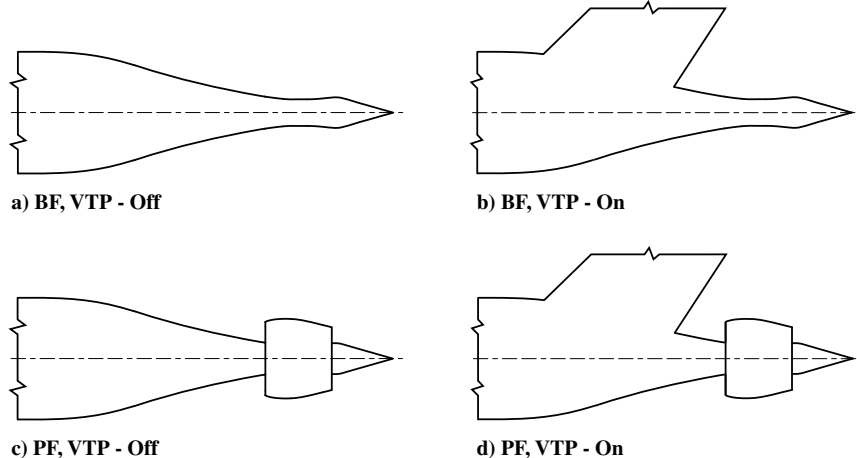


Fig. 7 Geometrical configurations tested in the wind-tunnel experiments.

between -6 and 12 deg, while the angle of sideslip β was varied between -8 and 8 deg. Balance measurements were carried out in several conditions, including cases in which both α and β were varied together. Contrarily, other measurements were carried out in conditions obtained by varying one of the angles, while the other was kept equal to zero. In addition, for the powered fuselage cases, the fan-tip-speed ratio, $U_{\text{tip}}/V_{\infty} = (1/2)\Omega D_f/V_{\infty}$, was varied by controlling the fan rotational speed Ω .

D. Momentum and Energy Analysis

The momentum and energy components in the flowfield were analyzed through the Power Balance Method [4] based on the total pressure and stereoscopic PIV measurements. The momentum and energy flow rates across the survey planes were evaluated through the definitions

$$F_x = \iint \left[(p_t - p_{\infty}) + \frac{1}{2}(u - V_{\infty})^2 - \frac{1}{2}(v^2 + w^2) \right] dS \quad (1)$$

$$\dot{E}_a = \iint \frac{1}{2} \rho u (u - V_{\infty})^2 dS \quad (2)$$

$$\dot{E}_v = \iint \frac{1}{2} \rho u (v^2 + w^2) dS \quad (3)$$

$$\dot{E}_p = \iint (p - p_{\infty})(u - V_{\infty}) dS \quad (4)$$

where F_x is the axial momentum flow rate; \dot{E}_a is the axial kinetic energy flow rate; \dot{E}_v is the transverse kinetic energy flow rate; \dot{E}_p is the pressure work rate; u , v , and w are the Cartesian velocity components; ρ is the flow density; p_t is the total pressure; and p is the static pressure.

The integrals were carried out over a circular survey plane S perpendicular to the freestream velocity direction. The integration domain extended up to $r = 0.8R_b$, to capture entirely the propulsor slipstream, the fuselage wake, and the fuselage-VTP junction flow. The momentum flow rate F_x is defined positive when corresponding to a momentum deficit and hence to a force component in the drag direction. In selected cases, to ease the interpretation of the results, F_a is defined as $F_a = -F_x$ and hence positive for a momentum excess and a force component in the thrust direction. The velocity components u , v , and w were directly measured through the stereoscopic PIV measurements, while the total pressure p_t was obtained from the pitot measurements. The effect of the probe incidence angle on the total pressure readings was corrected using the velocity data. For each probe position, the corresponding inflow angle was evaluated from the velocity field and used to correct the pitot measurement through the probe calibration curve. The calibration curve was measured by placing the probe in the freestream flow and by tilting it with respect

to the freestream velocity direction. Throughout the present analysis, the flow was assumed to be incompressible, and hence $\rho = \rho_\infty$. The static pressure p was computed from the stereoscopic PIV and pitot data through the incompressible Bernoulli equation.

III. Results

The aerodynamic performance of the Propulsive Fuselage Concept, resulting from the complex aerodynamic interactions occurring between the BLI propulsor and the airframe, was investigated through several measurement techniques. In this section, the main findings from the experimental study are presented and discussed. First, the effect of the BLI propulsor on the overall aircraft forces and

moments is discussed. Subsequently, the flowfield around the BLI propulsor is investigated in detail. Finally, the distribution of the momentum and power components in the flowfield is presented. The results discussed in this section are focussed on the aerodynamics of the PF configuration, while the performance of the BF configuration is discussed in the Appendix.

A. Effect of BLI Propulsor on Aerodynamic Forces and Moments

The effect of the BLI propulsor on the overall aircraft aerodynamic forces and moments was quantified in different operating conditions through the six-components external balance. Figure 8 presents the aerodynamic force and moment coefficients induced by the BLI propulsor as a function of the fan tip speed ratio U_{tip}/V_∞ . The

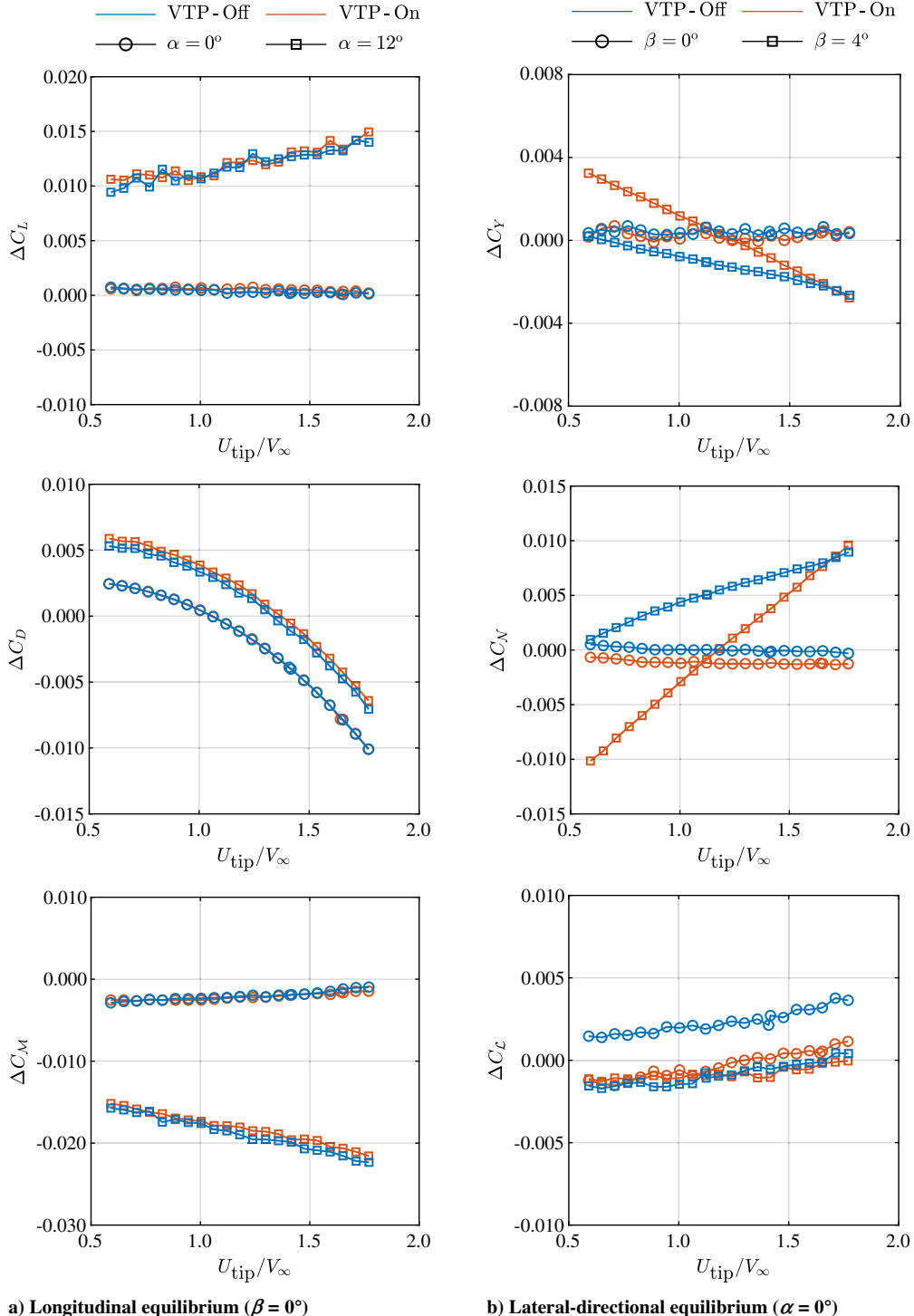


Fig. 8 Effect of the BLI propulsor on the aerodynamic forces and moments coefficients. Balance measurements taken at $Re_c = 460,000$.

propulsor-induced components were obtained by subtracting the values measured for the BF case from those measured for the PF case ($\Delta C_0 = C_0^{\text{PF}} - C_0^{\text{BF}}$). These ΔC_0 components account for the effects of the fan and of the shroud. The results of the balance measurements for the BF configuration are presented in Fig. A1 of the Appendix. Figure 8a reports the propulsor-induced lift, drag, and pitching moment coefficients, respectively, ΔC_L , ΔC_D , and ΔC_M , at $\beta = 0$ deg and $\alpha = 0$ deg and 12 deg. The measurements show the following:

1) C_L is not affected by the propulsor installation and operating condition at $\alpha = 0$ deg. At $\alpha = 12$ deg, C_L slightly increases ($\Delta C_L \leq 0.01 C_L^{\text{BF}}$) due to the lift produced by the shroud and the component of the fan thrust in the lift direction.

2) C_D changes significantly due to the propulsive unit installation. At $\alpha = 0$ deg, the added drag due to the shrouded fan was compensated by the propulsor at around $U_{\text{tip}}/V_{\infty} = 1$, at which $C_D^{\text{BF}} = C_D^{\text{PF}}$. The addition of the VTP contributes to the drag increase, but it is not significantly influenced by the fan installation and settings. A consistent behavior is found at $\alpha = 12$ deg, although higher drag is measured relatively to the respective BF case at a given $U_{\text{tip}}/V_{\infty}$. This is due to the higher drag produced by the shroud and to the composition of the thrust in the lift and drag directions.

3) C_M is unaffected by the propulsor installation and setting at $\alpha = 0$ deg. However, at $\alpha = 12$ deg, the fan installation introduces a nosedown contribution to C_M , due to the lift produced by the shroud contour and to the onset of an in-plane force component on the fan. The nosedown effect increases in magnitude for increasing $U_{\text{tip}}/V_{\infty}$, suggesting that the fan in-plane force and the shroud lift increase at higher fan thrust settings.

Figure 8b reports the propulsor-induced side force, yawing, and rolling moment coefficients, respectively, ΔC_Y , ΔC_N , and ΔC_L , at $\alpha = 0$ deg and $\beta = 0$ deg and 4 deg. The measurements show the following:

1) ΔC_Y is small at $\beta = 0$ deg due to the symmetric flow conditions, and the effect of the fan is negligible. However, at $\beta = 4$ deg, C_Y slightly decreased (increased in magnitude) for increasing $U_{\text{tip}}/V_{\infty}$, due to an increase in magnitude of the side force produced by the shroud and of the in-plane fan force. Comparing the VTP-off and VTP-on data, it can be seen that the presence of the tail affected the side force produced by the propulsor unit, which resulted in a change in slope of the ΔC_Y curve.

2) ΔC_N shows a behavior which is consistent with that of ΔC_Y . ΔC_N is small at $\beta = 0$ deg and is not affected by the fan, due to the symmetric flow conditions. At $\beta = 4$ deg, the onset of the side force on the propulsor introduces a positive yawing moment contribution, which increases with $U_{\text{tip}}/V_{\infty}$. As noted for ΔC_Y , the interaction with the VTP results in an increased slope of the curve in the VTP-on case.

3) The effect of the fan installation and setting on C_L is negligible both at $\beta = 0$ deg and $\beta = 4$ deg. The small increase seen in ΔC_L at $\beta = 0$ deg for increasing $U_{\text{tip}}/V_{\infty}$ might be due to the increasing torque induced by the fan on the outlet vanes.

B. Distortions of BLI Propulsor Inflow Field

Figure 9 shows the total pressure coefficient C_{p_t} measured upstream of the shroud inlet for the PF case at various incidence conditions. In the PF cases, the propulsor was operated at $U_{\text{tip}}/V_{\infty} = 1.7$. Moreover, for the cruise conditions ($\alpha = \beta = 0$ deg), both VTP-on and VTP-off cases are shown. Figures 9a and 9b show that in cruise conditions the fuselage boundary layer introduces total pressure gradients in the radial direction. In particular, at the survey plane location, the boundary-layer thickness is approximately $0.65 R_b$. In both VTP-off and VTP-on cases, the bottom sector of the plot ($|\phi| > 120$ deg) is affected by the influence of the fuselage support strut (region A). The vertical tail plane introduces a nonuniform p_t distribution (region B), which is due to two sources: the viscous wake of the tail, introducing a narrow and relatively strong p_t deficit (approximately for -5 deg $< \phi < 5$ deg), and the junction flow, introducing a wide and relatively weak p_t deficit close to the fuselage wall (approximately for -30 deg $< \phi < 30$ deg).

The inflow total pressure was measured at $\alpha = 12$ deg and $\beta = 0$ deg to simulate conditions representative of takeoff or top-of-climb maneuvers. Figure 9c shows the p_t distribution for the PF, VTP-on case. The increased incidence angle results in the onset of a crossflow around the fuselage section (see, for example, Refs. [35,36]). This crossflow displaces the lower p_t flow farther from the fuselage on the leeward side (region C), while higher p_t flow is entrained on the windward side (region D). The VTP causes a p_t deficit due to its viscous wake similarly to the $\alpha = 0$ deg case (region E). However, the junction flow distortion is not clearly visible anymore close to the fuselage contour. This could be a consequence of the crossflow component that displaces the horseshoe vortex further from the surface.

Figure 9d reports the fan-inflow total pressure for $\alpha = 0$ deg and $\beta = 4$ deg for the PF, VTP-on case. Similarly to the case at $\alpha = 12$ deg, due to the crossflow component around the fuselage contour, the low-momentum fluid is displaced on the leeward side (region F), while higher p_t flow is entrained on the windward side (region G). Moreover, the vertical tail produces a strong asymmetric distortion, which is enhanced by the fact that the tail is producing lift under the sideslip β . In particular, a low p_t region is found on the leeward side (corresponding to the suction side of the vertical tail) in proximity of the fuselage body (region H), presumably due to trailing-edge separation. In fact, inside the fuselage boundary layer, the effective incidence angle of the tail sections are most likely higher than the sideslip angle, due to the lower axial velocity component. On the windward side (corresponding to the pressure side of the vertical tail), the p_t distribution typical of a horseshoe vortex can be identified, as a result of the junction flow developing at the tail-fuselage intersection (region I). Consequently, strong pressure gradients are found in the azimuthal direction around $\phi = 0$ deg.

The total pressure distribution at the fan inlet found in cruise conditions, displayed in Fig. 9b, was decomposed in the three basic components associated to the fundamental aerodynamic phenomena that cause them, namely, the fuselage boundary layer, the VTP wake, and the junction flow. The results of the decomposition are reported in Fig. 10. Note that the total pressure measurements were done only for 0 deg $\leq \phi \leq 180$ deg and then mirrored for visualization purposes. Moreover, the distortions induced by each of these components were summarized through the standard distortion parameters DC(60), CDI and RDI, and are gathered in Table 2. The parameters were defined as (see Ref. [37])

$$\text{DC}(60) = \frac{p_t^{\text{avg}} - p_{t,60 \text{ deg}}^{\text{avg}}}{p_t^{\text{avg}}} \quad (5)$$

$$\text{CDI} = \max_r \left(\frac{p_t^{\text{avg}}(r) - p_t^{\text{min}}(r)}{p_t^{\text{avg}}} \right) \quad (6)$$

$$\text{RDI} = \max \left(\frac{p_t^{\text{avg}} - p_t^{\text{avg}}(r_{\text{min}})}{p_t^{\text{avg}}}, \frac{p_t^{\text{avg}} - p_t^{\text{avg}}(r_{\text{max}})}{p_t^{\text{avg}}} \right) \quad (7)$$

where p_t^{avg} is the average total pressure value in the survey plane (360 deg), $p_{t,60 \text{ deg}}^{\text{avg}}$ is the minimum average total pressure value in a sector of 60 deg, $p_t^{\text{avg}}(r)$ is the average total pressure value at the radial position r , and $p_t^{\text{min}}(r)$ is the minimum total pressure value at the radial position r .

The momentum distribution C_{p_t} , shown in Fig. 10a, is primarily the result of the flow around the fuselage, vertical tail, and their mutual interaction and is a function of both r and ϕ , in other words, $C_{p_t} = F(r, \phi)$.

F_1 , shown in Fig. 10b, represents the momentum deficit due to the fuselage boundary layer, and it was directly measured on the VTP-off configuration. Ideally, for an axisymmetric fuselage at zero incidence, and neglecting the effect of the wings, F_1 would be a function of r and constant with ϕ . In practice, due to the lifting wings and the interference of the fuselage support strut, the measured F_1 deviates from an axisymmetric condition.

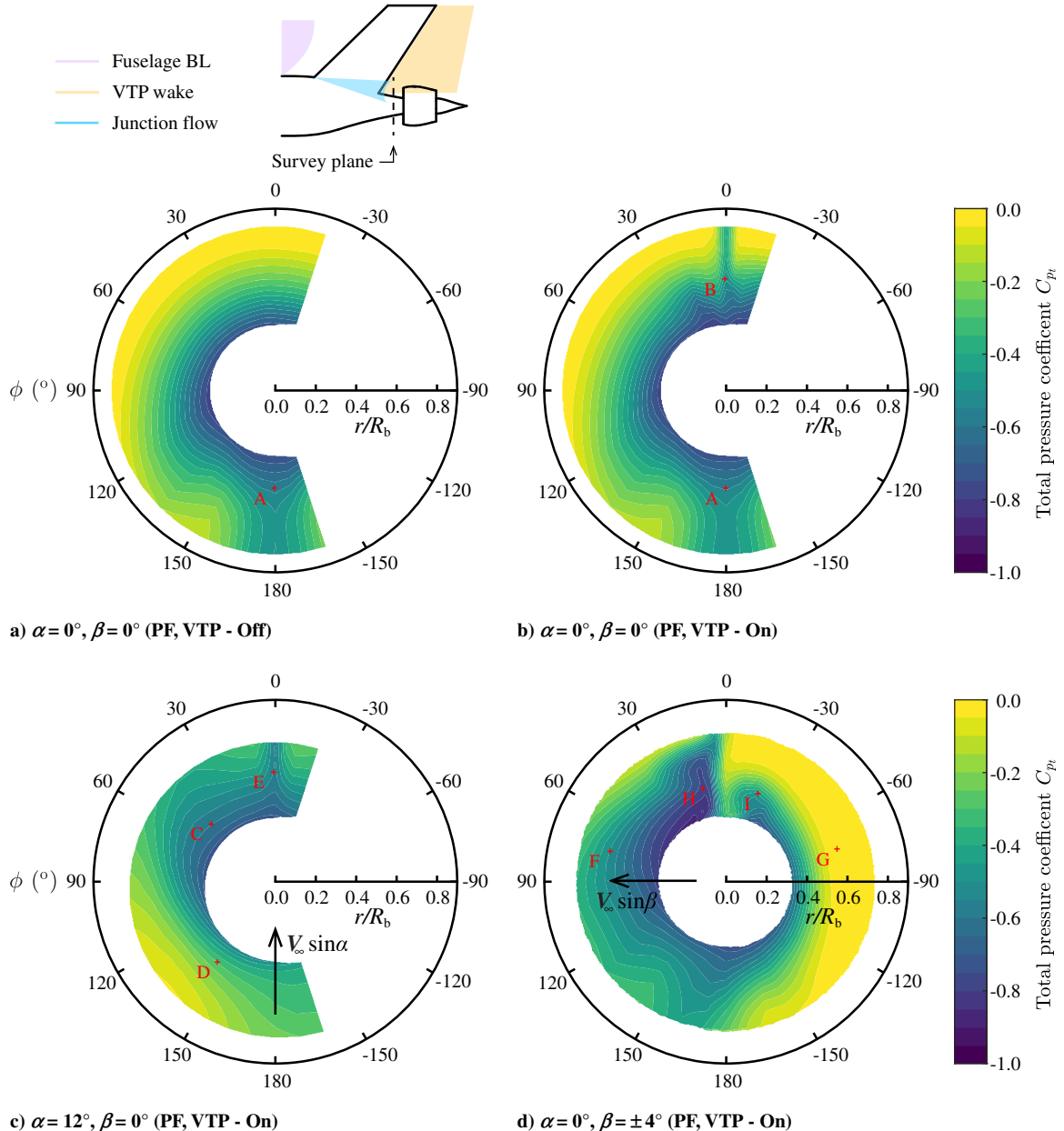


Fig. 9 Total pressure distributions upstream of the BLI propulsor for the PF case at various incidence angles (back view). Arrows indicate the direction of the crossflow component. Total pressure measurements taken at $Re_c = 460,000$ and $U_{tip}/V_\infty = 1.7$.

Furthermore, the total pressure distribution component due to the tail installation was isolated by subtracting the VTP-on and VTP-off cases, and it is reported in Fig. 10c. This component can be further decomposed in two parts: F_2 , representing the viscous wake of the VTP, and F_3 , representing the effect of the tail-fuselage junction flow. To obtain F_2 , first the uninstalled tail wake F'_2 , reported in Fig. 10d, was estimated. F'_2 represents the momentum deficit distribution in the wake of the VTP operating in uniform freestream flow (hence without the effect of the fuselage boundary layer). F'_2 was estimated by assuming a C_{p_t} profile equal in shape to the profile that was measured outside of the fuselage boundary layer ($r/R_b = 0.795$). At each radial position r , this C_{p_t} profile was scaled proportionally to the local VTP chord length. This is valid in the assumption that the section drag scales linearly with the section chord length. Subsequently, the installed tail wake F_2 , reported in Fig. 10e, was obtained by scaling F'_2 with the local total pressure ratio $p_t/p_{t\infty}$ in order to take into account the nonuniform dynamic pressure impinging on the different VTP sections. This is valid in the assumption that radial static pressure gradients can be neglected in the fuselage boundary layer. F_2 results in a p_t deficit concentrated

around the center of the VTP ($-5^\circ < \phi < 5^\circ$) and nonlinearly decreasing in intensity toward the fuselage wall. Finally, F_3 , reported in Fig. 10f, was obtained as complementary of F_2 to the total tail installation effect. F_3 is strongly two-dimensional and characterized by a low total pressure region coincident with the core of the horseshoe vortex.

The decomposition of C_{p_t} clearly shows that the total momentum deficit characterizing the BLI fan inflow can be obtained as a combination of elementary components associated with well-defined physical sources of momentum deficit. Comparing the different elements, it can be concluded that the lowest p_t values are induced by the fuselage boundary layer (Fig. 10b). However, because this deficit is approximately axisymmetric, it does not induce nonuniform disk loads, and the design of the BLI propulsor can be adapted to sustain the distortion with minor performance penalties (see, for example, Ref. [16]). On the contrary, the inlet distortions induced by the tail installation will induce nonuniform disk loads and hence potentially affect the aeroacoustic and aeromechanical performance of the BLI fan [25,26]. This qualitative analysis is supported by the distortion parameters reported in Table 2. In fact, it can be observed

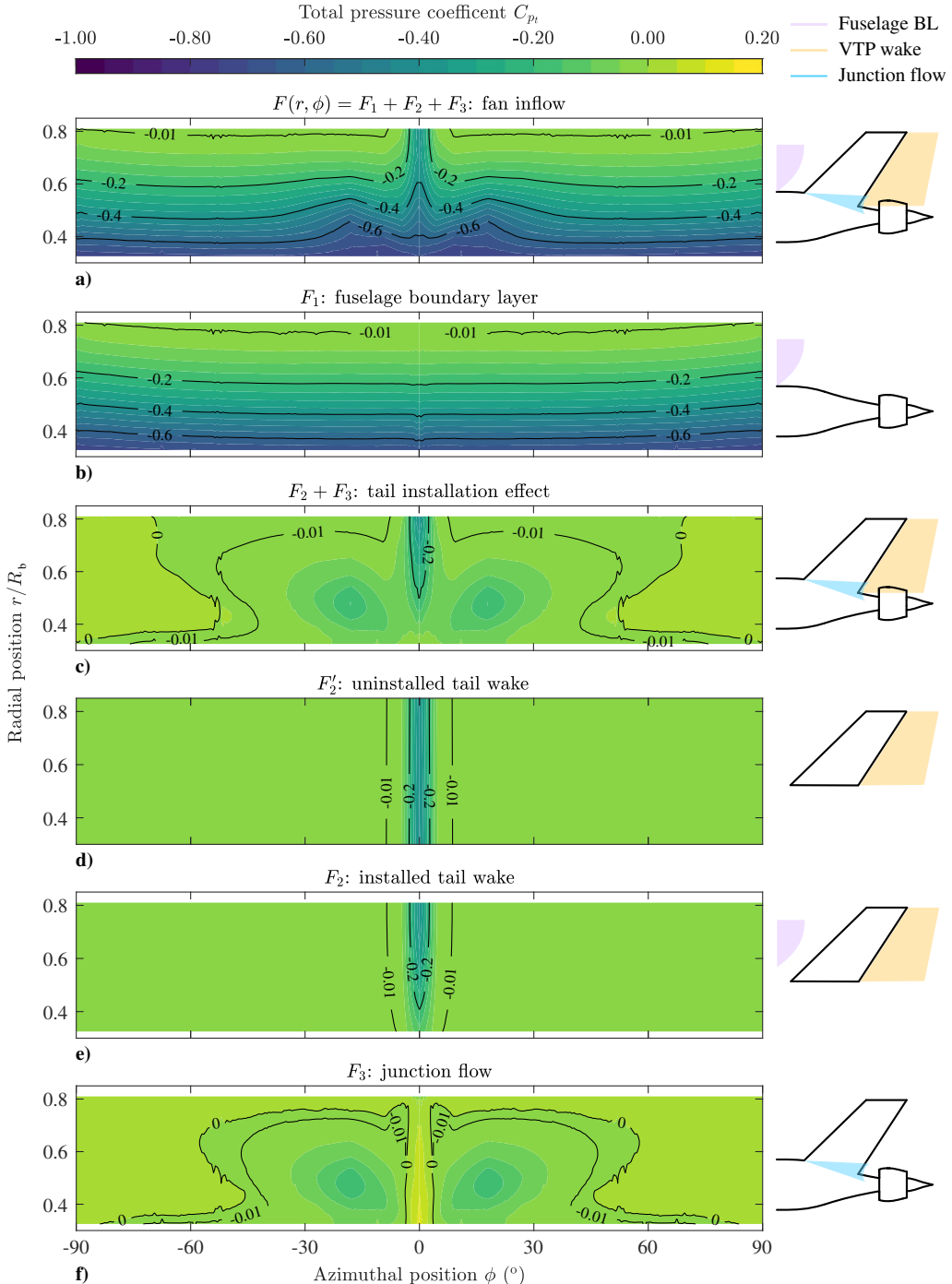


Fig. 10 Fundamental components of the fan inflow total pressure distribution in cruise conditions. Total pressure measurements taken at $\alpha = 0$ deg $\beta = 0$ deg, $U_{\text{tip}}/V_{\infty} = 1.7$, and $Re_{\bar{c}} = 460,000$.

Table 2 Inlet distortion metrics for the fundamental components of the fan inflow total pressure distribution in cruise conditions (F : fan inflow; F_1 : fuselage boundary layer; F_2 : installed tail wake; F_3 : junction flow; total pressure measurements taken at $\alpha = 0$ deg $\beta = 0$ deg, $U_{\text{tip}}/V_{\infty} = 1.7$, and $Re_{\bar{c}} = 460,000$)

Parameter	F	F_1	F_2	F_3
DC(60)	0.06	0.03	0.02	0.04
CDI	0.85	0.10	0.39	0.20
RDI	0.66	0.63	0.01	0.01

that the momentum deficit due to the fuselage boundary layer F_1 contributes with the highest RDI coefficient, while the VPT wake F_2 is characterized by the highest CDI coefficient. Overall, the DC(60) values measured are relatively low due to the facts that the axisymmetric component of the inlet distortions F_1 is dominant and the strongest nonaxisymmetric component of the distortions F_2 is concentrated in a narrow sector.

Stereoscopic PIV measurements were carried out in a plane perpendicular to the freestream direction at $x/L_b = 0.89$ to quantify the velocity field at the shroud inlet in cruise conditions (see Sec. II.B.3). Figure 11 reports the three velocity components u , v , and w , together with the swirl angle θ and the axial vorticity component ω_x for the BF, VTP-on configuration.

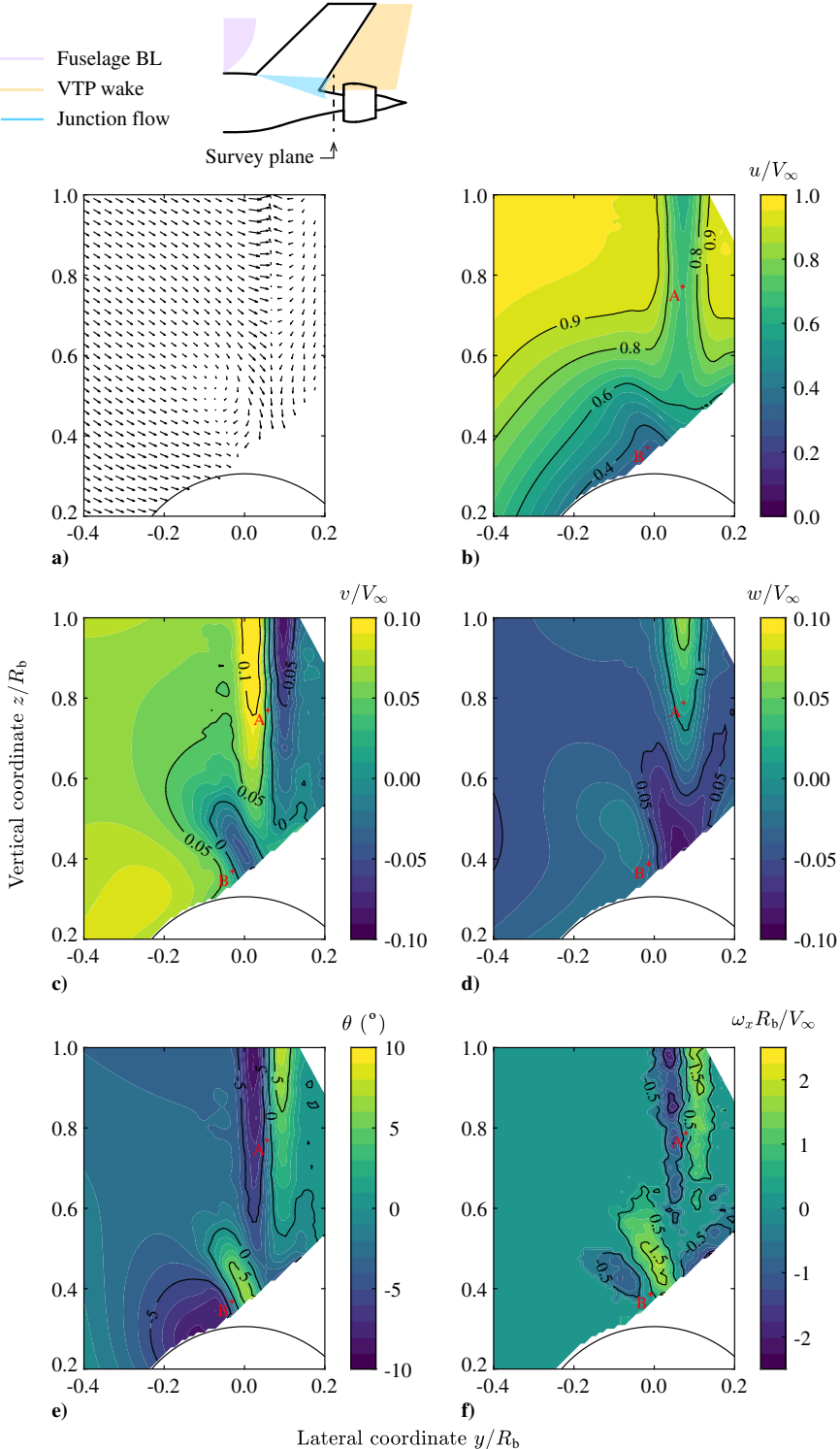


Fig. 11 Flowfield at $x/L_b = 0.89$ for the BF, VTP-on configuration (back view). Stereoscopic PIV measurements for $\alpha = 0$ deg = $\beta = 0$ deg and $Re_c = 460,000$.

Figure 11b displays the axial velocity contour, which, similarly to the C_{p_t} in Fig. 9b, is characterized by the fuselage boundary layer, VTP wake (region A) and junction flow (region B). The VTP influences the fan inflow field with in-plane velocity components, which can be easily visualized in Fig. 11a. In fact, in the VPT wake, the lateral velocity component v is directed toward the center of the wake itself (Fig. 11c) due to the wake contraction. Moreover, a positive vertical (spanwise) velocity component w is found (Fig. 11d). This vertical flow, directed from the root to the tip of the tail, is due to the onset of a crossflow component in the tail

boundary layer induced by the leading-edge sweep. These v and w distributions have two direct consequences on the fan inflow. First, downstream of the tail plane, a velocity tangent to the fan plane is induced, which is corotating with the blades on the approaching-blade side (in this case, the left-hand side) and counterrotating on the retreating-blade side (in this case, the right-hand case). This results in a swirl angle θ displayed in Fig. 11e, peaking at around ± 8 deg in the VPT wake. Second, the vertical crossflow in the VTP boundary layer introduces streamwise vorticity ω_x that is transported downstream and ingested by the fan (Fig. 11f).

C. Flowfield Downstream of BLI Propulsor

The flowfield downstream of the BLI propulsor was quantified through total pressure and stereoscopic PIV measurements on a survey plane perpendicular to the freestream velocity direction located at the fuselage trailing edge (plane at $x/L_b = 1$ of Fig. 6). The measurements were carried out at $\alpha = \beta = 0$ deg and at $U_{\text{tip}}/V_{\infty} = 1.7$. The distributions of total pressure p_t , axial velocity velocity u , tangential velocity v_t , and axial vorticity ω_x are reported in Fig. 12.

The fan slipstream clearly shows a total pressure and axial velocity higher than the freestream (Figs. 12a and 12b, respectively). The low total pressure and velocity region around the fuselage axis is due to the onset of a vortical structure around the fuselage hub. This structure, induced by the fan slipstream, was analyzed in detail in a previous related work [22]. Furthermore, C_{p_t} and u show a nonaxisymmetric distribution over the entire slipstream annulus. In particular, the wakes of the outlet vanes (see Fig. 13) are visible, as they are characterized by a relatively lower total pressure and axial velocity.

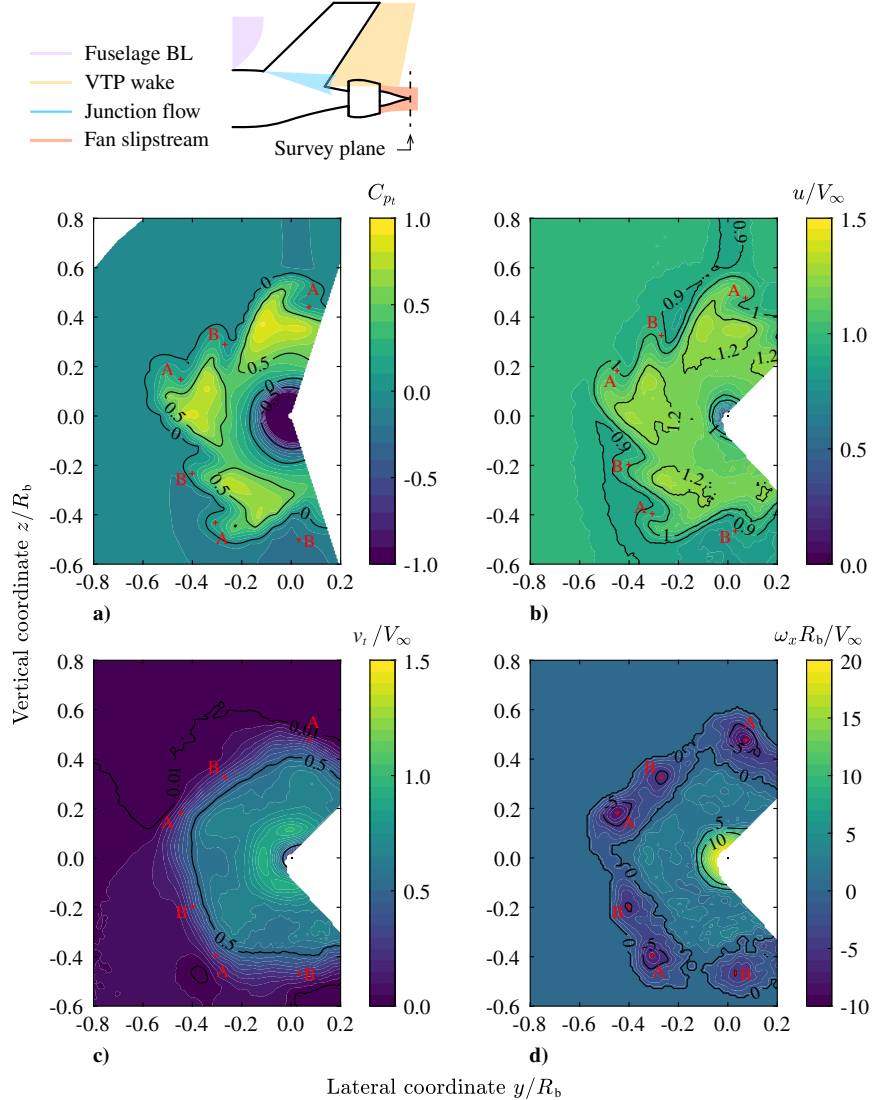


Fig. 12 Flowfield at $x/L_b = 1$ for the PF, VTP-on configuration (back view). Total pressure and stereoscopic PIV measurements for $\alpha = 0$ deg $= \beta = 0$ deg, $U_{\text{tip}}/V_{\infty} = 1.7$, and $Re_{\tilde{c}} = 460,000$.

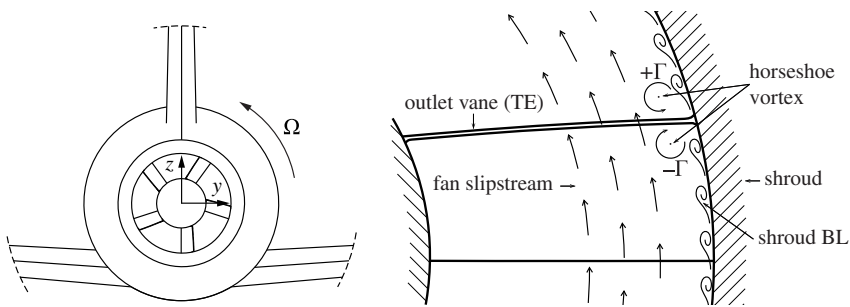


Fig. 13 Schematic of the flow interactions between the fan slipstream and the viscous flow around the vane and shroud surfaces.

Moreover, the outer region of the slipstream is affected by the presence of streamwise vortices (Fig. 12d) which induce the structures labeled as A and B in Fig. 12. These vortices are thought to be due to the interactions between the shroud–vanes junction flow and the fan slipstream, as sketched in Fig. 13. The horseshoe vortex generated at the intersection between the outlet and inlet vanes and the shroud results in five pairs of counterrotating vortices, corresponding to the vortices A and B, respectively. These

vortices are convected downstream in the fan slipstream, hence following an helical trajectory. The viscous interaction with the swirling flow in the fan slipstream results in an enhanced dissipation of the corotating $+\Gamma$ filament while keeping the counter-rotating filament $-\Gamma$ stable. It must be noted that, though consistent with the experimental observations, no experimental data are available to directly validate the proposed phenomena. A more detailed investigation of the flowfield is required through

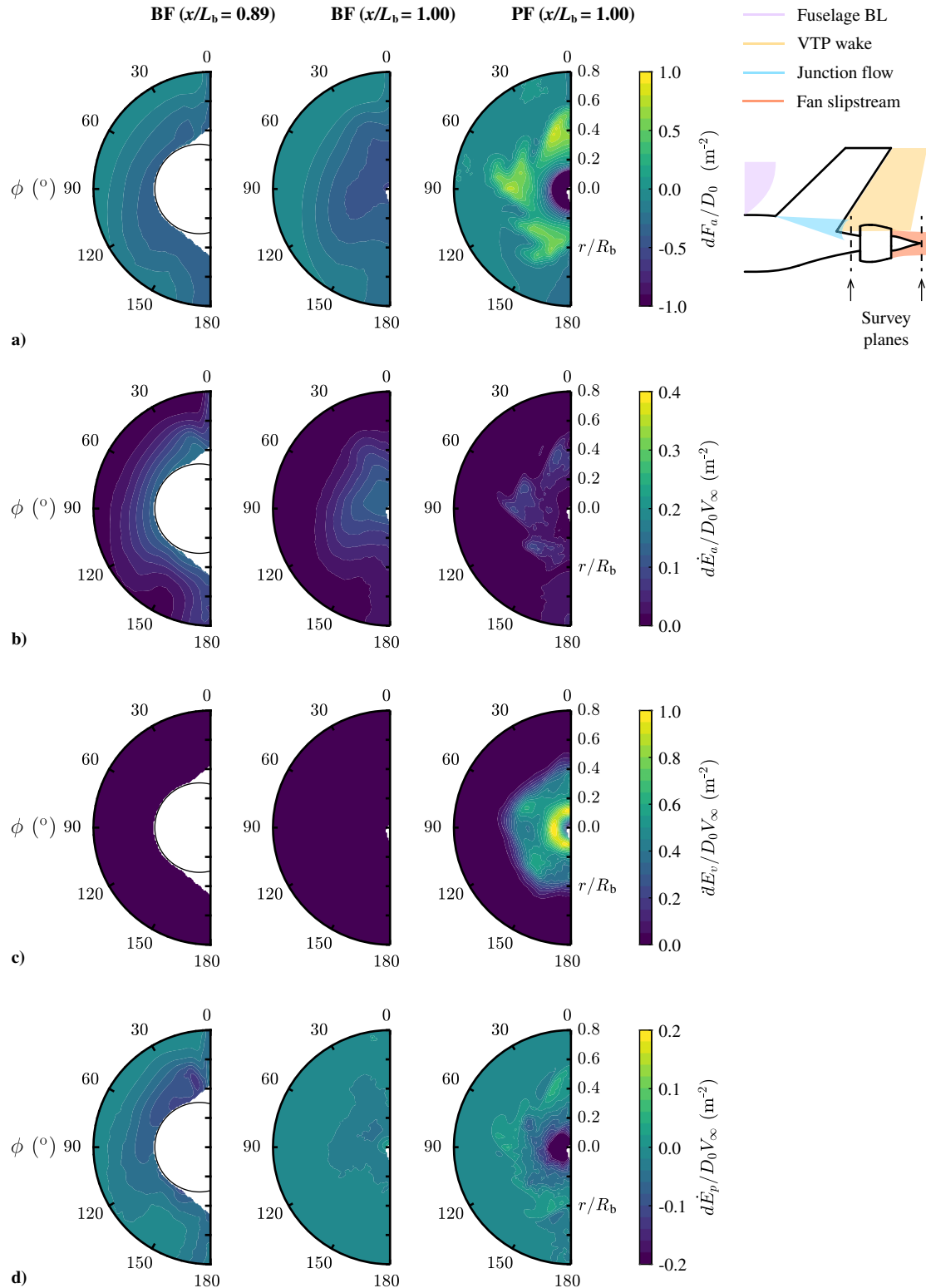


Fig. 14 Distributions of the momentum and energy flux densities at $x/L_b = 0.89$ and $x/L_b = 1.00$ for the BF, VTP-on and PF, VTP-on cases (back view). Total pressure and stereoscopic PIV measurements for $\alpha = 0$ deg = $\beta = 0$ deg, $U_{tip}/V_\infty = 1.7$ (PF case), and $Re_\tau = 460,000$.

dedicated measurements of numerical analysis, possibly with time-resolved flow data.

Finally, the tangential velocity component v_t (Fig. 12c) has a uniform distribution in the center of the fan slipstream and strongly increases toward the hub region due to the presence of the hub vortex.

D. Flow Momentum and Power Analysis

The total pressure and velocity data were combined to estimate the main momentum and power fluxes across a survey plane perpendicular to the flow and positioned at $x/L_b = 0.89$ and at $x/L_b = 1$ for the BF and PF configurations. The terminology, main equations, and procedures used are discussed in Sec. II.D. Figure 14 reports the distribution of the momentum and power flux densities in the survey planes. The fluxes dF_a , $d\dot{E}_a$, $d\dot{E}_v$, and $d\dot{E}_p$ represent the amount of momentum or power transported through the survey plane per unit area, and their surface integral is equal to the respective flow rates F_x , \dot{E}_a , \dot{E}_v , and \dot{E}_p defined in Sec. II.D. The momentum and power flux densities were expressed as ratio to D_0 and D_0V_∞ , respectively, where D_0 is the measured drag of the BF, VTP-on case at $\alpha = \beta = 0$ deg. Therefore, the momentum and power terms were related to a reference drag and drag power associated to the baseline aircraft configuration. In particular, in the calculation of D_0 the drag of the fuselage strut was estimated through a two-dimensional (2-D) viscous flow solver (XFOIL, Ref. [38]) and subtracted from the balance measurements.

Figure 14a shows the momentum flux density, $dF_a = -dF_x$, which is positive for a local momentum excess and negative for a local momentum deficit. Clearly, for the BF cases, dF_a shows a momentum deficit in the fuselage boundary layer and in the wake of the VTP on both survey planes. For the PF configuration, a momentum excess is found in the fan slipstream, while a strong momentum deficit is measured around the fuselage axis due to the onset of the vortical flow already discussed. Similarly, the axial kinetic energy flux density, $d\dot{E}_a$ in Fig. 14b, shows that for the BF case the kinetic energy flux is concentrated in the regions of momentum deficit (i.e., the fuselage boundary layer and the VTP wake). However, for the PF case, $d\dot{E}_a$ shows relatively low values thanks to the axial velocity induced by the BLI fan. Contrarily, as shown in Fig. 14c, the transverse kinetic energy flux density $d\dot{E}_v$ is relatively low for the BF cases. For the PF case, the swirl velocity induced by the fan resulted in a strong $d\dot{E}_v$, which reaches the maximum values in the vortical flow region around the fuselage axis. Finally, the pressure work flux, $d\dot{E}_p$ in Fig. 14d, shows that for the BF case the flow is expanded in the fuselage boundary layer at $x/L_b = 0.89$ and that the static pressure recovers substantially already at $x/L_b = 1$. For the PF case, the static pressure slightly exceeds the freestream value in the fan slipstream, while very low pressure is found the vortical structure around the fuselage axis.

Figure 15 reports the momentum and energy flow rates obtained as surface integrals of the flux densities reported in Fig. 14. As already discussed, the momentum and power terms are expressed in terms of D_0 and D_0V_∞ . It can be seen that for the BF case at $x/L_b = 0.89$ a momentum flow rate equal to approximately 16% of the total aircraft drag was measured in the survey plane. Moreover, F_x increased to almost 20% of D_0 at $x/L_b = 1$. This suggests that a substantial share of momentum in the fuselage boundary layer (around 20–25%), associated to the fuselage body drag, is dissipated in the flow around the contracting aft cone of the fuselage body. This shows very good consistency with the results of a related study focussed on the study of the same fuselage geometry in a 2-D axisymmetric setup [22].

The kinetic energy flow rate \dot{E}_a shows an opposite variation when moving from $x/L_b = 0.89$ to $x/L_b = 1$ for the BF case, resulting in around 25% lower flow rate at the trailing edge. This is due to the contributions to \dot{E}_a found in the wakes of the VTP and of the fuselage support strut which are clearly visible at $x/L_b = 0.89$ and are much weaker at $x/L_b = 1$. In fact, the results of a previous related work (Ref. [22]) have shown that, for the same fuselage geometry without the VTP and the fuselage strut, \dot{E}_a has a similar value at $x/L_b = 0.89$

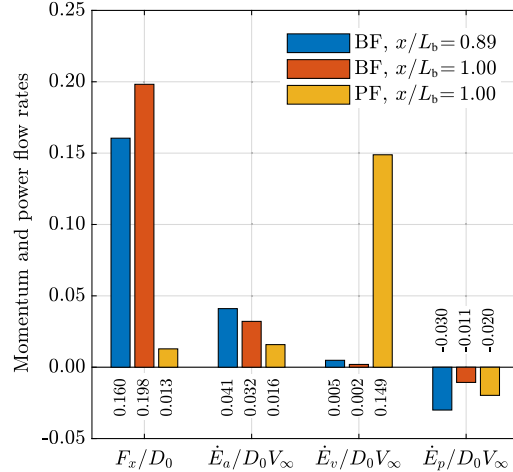


Fig. 15 Integral momentum and energy flow rates at $x/L_b = 0.89$ and $x/L_b = 1.00$ for different fuselage configurations. Measurements for $\alpha = 0$ deg = $\beta = 0$ deg.

and $x/L_b = 1$. For the PF case, the value of \dot{E}_a was effectively reduced of around 50% at $x/L_b = 1$ compared to the BF case. The analysis of \dot{E}_a shows that, first, around 3–4% of the total aircraft drag power D_0V_∞ is transported and dissipated in the wake of the aircraft; these values represent the ideal power benefit that could be achieved with a so-called ideal BLI propulsor (see Ref. [4]). Moreover, the acceleration imposed by the BLI fan on the low-momentum fuselage boundary layer effectively reduces \dot{E}_a and hence the wake dissipation.

The transverse kinetic energy flow rate \dot{E}_v shows very small values for the BF cases, due to the relatively small in-plane velocity components. On the contrary, \dot{E}_v is the dominant factor for the PF case, due to the relatively strong swirl component in the fan slipstream. This component can be mitigated with an accurate design of the outlet vanes to recover the swirl velocity induced by the fan stage. Finally, the pressure work rate \dot{E}_p shows a negative value for the BF cases, due to the fact that the flow accelerates (decreasing pressure) due to the fuselage curvature. The expanded flow then undergoes a compression (increasing pressure) around the contracting aft cone toward the trailing edge and the associated pressure recovery results in a decreasing (in magnitude) pressure work rate at $x/L_b = 1$. The decrease in \dot{E}_p for the PF case due to the BLI fan is due to the low static pressure found in the core of the vortical flow around the fuselage axis (see again Fig. 14d).

IV. Conclusions

This paper has presented an experimental analysis of an aircraft featuring a fuselage-mounted boundary-layer ingesting propulsor representative of the CENTRELINe Propulsive Fuselage Concept. The wind-tunnel tests were carried out in the low-speed wind-tunnel facilities of Delft University of Technology. The measurements were performed at a mean-chord-based Reynolds number of 460,000 and a Mach number of 0.12. As a reference, in full-scale cruise conditions, the Reynolds and Mach numbers would be 40,000,000 and 0.82, respectively.

The goals of the experiment were 1) to study the effect of the fuselage-mounted BLI propulsor on the overall-aircraft aerodynamic forces and moments in all flight conditions and 2) to characterize the flowfield around the BLI propulsor and the aerodynamic interactions occurring between the propulsor and the airframe.

The analysis of the experimental data shows the following:

1) In cruise conditions ($\alpha = \beta = 0$ deg and $U_{tip}/V_\infty = 1.7$), the effect of the BLI propulsor on the aircraft forces and moments is mostly limited to the thrust–drag equilibrium. However, at incidence, the BLI propulsor showed a nonnegligible effect on both longitudinal and lateral-directional equilibrium.

2) In cruise conditions, the fuselage boundary layer represents the strongest distortion to the fan inflow, while the influence of the wing lift and downwash is secondary. The VTP introduces a total pressure deficit, which can be decomposed in two contributions: the VTP viscous wake, with a restricted azimuthal extension ($-5 \text{ deg} < \phi < 5 \text{ deg}$), and the horseshoe vortex structure that develops at the fuselage-tail junction. The VTP wake induces in-plane velocity components, associated with the wake contraction and spanwise crossflow, which create nonnegligible swirl at the BLI propulsor inlet.

3) In off-design conditions ($\alpha, \beta \neq 0 \text{ deg}$), the crossflow component around the fuselage contour introduces a nonaxisymmetric distortion characterized by low total pressure on the leeward side and high total pressure on the windward side. At $\beta = 4 \text{ deg}$, the

vertical tail strongly affects the inflow field as it produces lift under the sideslip. The associated total pressure distortion is characterized by sharp gradients in the azimuthal and radial directions.

4) The BLI propulsor strongly alters the flow around the fuselage aft section. The flowfield is characterized by regions of relatively high momentum (fan slipstream) and low momentum (hub vortex).

5) An axial momentum flow rate equal to 16 and 20% of the total aircraft drag was estimated at $x/L = 0.89$ and $x/L = 1$, respectively, which represent the drag force associated to the fuselage body and VTP root section. Moreover, the axial kinetic energy flow rate \dot{E}_a varied from 4 to 3% of the aircraft drag power $D_0 V_\infty$ across the same planes. This indicates that a power savings of around 3–4% could be achieved through an ideal BLI propulsor.

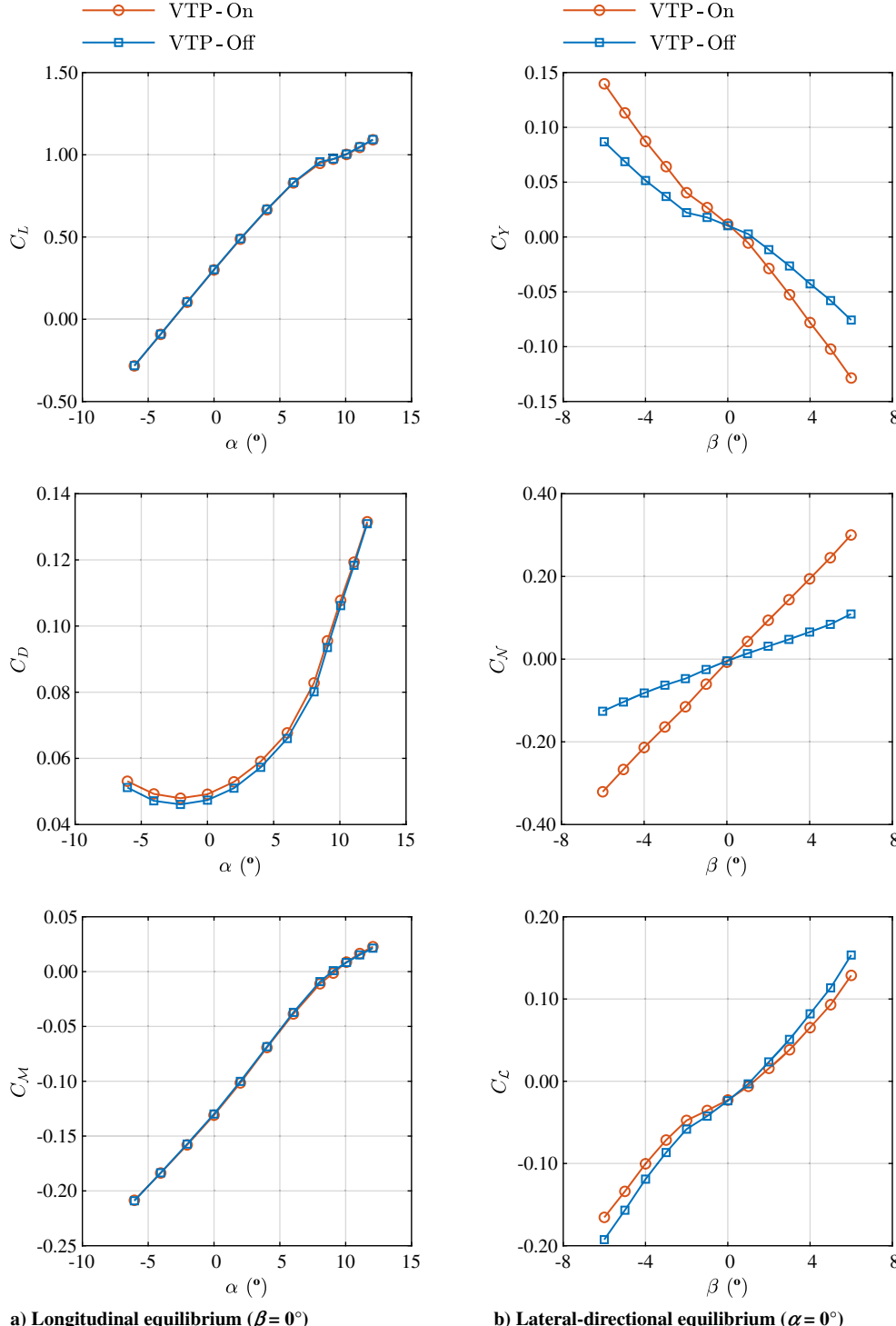


Fig. A1 Aerodynamic forces and moments coefficients on the bare fuselage configuration. Balance measurements taken at $Re_\epsilon = 460,000$.

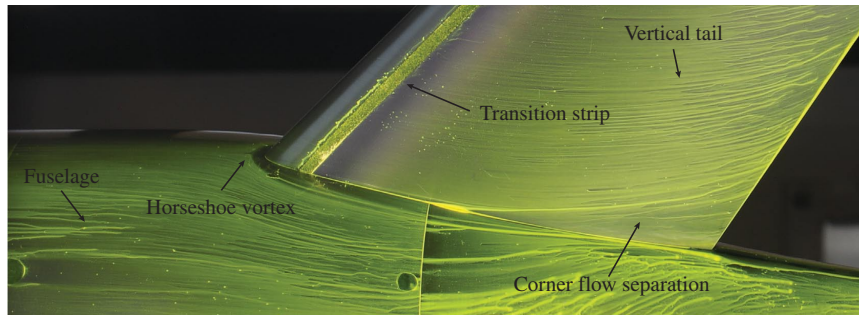


Fig. A2 Surface flow at the fuselage-tail intersection for the bare fuselage configuration in cruise conditions. Oil-flow measurements taken at $\alpha = 0$ deg = $\beta = 0$ deg and $Re_{\tilde{c}} = 460,000$.

6) The axial momentum and kinetic energy flow rates at the fuselage trailing edge are substantially reduced by the BLI propulsor, suggesting that the acceleration induced on the boundary-layer flow by the BLI propulsor effectively decreases \dot{E}_a and hence the dissipation occurring in the aircraft wake. However, in the investigated setup, only 50% of the available axial kinetic energy flow rate was recovered by the BLI fan.

Appendix: Performance of Bare Fuselage Configuration

This section provides a brief analysis of the aerodynamic performance of the BF configuration. External balance measurements were taken to investigate the aerodynamic forces and moments acting on the overall configuration at various operating conditions. Figure A1 shows the coefficients for varying incidence angle (Fig. A1a) and sideslip angle (Fig. A1a). The coefficients presented here take into account the forces and moments acting on the entire aircraft model, the fuselage support strut, and the exposed section of the wing struts.

Figure A1a shows the following:

1) C_L increases linearly for $\alpha < 8$ deg, after which a nonlinear behavior is found, probably due to the onset of flow separation on the wings. The tail installation has no meaningful effect on C_L .

2) C_D shows the expected quadratic trend against α , centered around the zero-lift angle. The tail installation increases the C_D with a bias that decreases with α . It must be noted that the aft-cone shape of the BF configuration was obviously not optimized for unpowered (i.e., propulsor-off) conditions. As a consequence, the fuselage aerodynamic performance in the BF configuration is penalized when compared to a conventional aft-cone design. However, the drag penalty due to the BF aft-cone design with respect to a conventional aft-cone shape was quantified to be less than 1% [32].

3) C_M linearly increases for $\alpha < 8$ deg, similarly to C_L . The tail installation has a negligible effect on C_M .

Figure A1b shows the following:

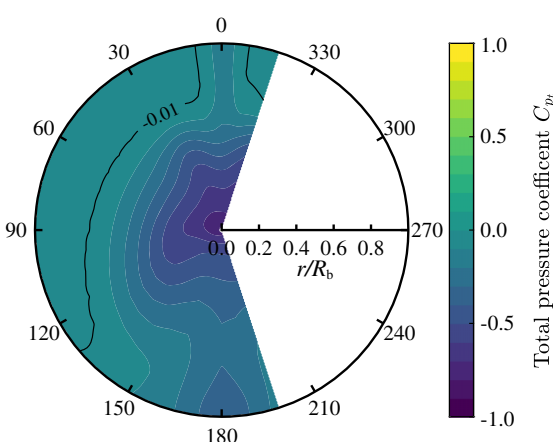


Fig. A3 Total pressure distribution at $x/L = 1$ for the BF, VTP-on case (back view). Total pressure measurements at $\alpha = 0$ deg = $\beta = 0$ deg and $Re_{\tilde{c}} = 460,000$.

1) C_Y nonlinearly increases in modulus with β . Similarly, the VTP contribution linearly increases with β .

2) C_N linearly increases with β . The contribution of the VTP also linearly increases with β , due to the side force produced by the VTP.

3) C_L nonlinearly increases with β . The contribution of the VTP reduces C_L , due to the side-force on the VTP.

To identify the main surface flow features at different operating conditions, the surface flow on the fuselage aft cone and vertical tail was visualized with a fluorescent oil-flow visualization. Figure A2 shows the surface flow for the BF configuration in cruise conditions ($\alpha = \beta = 0$ deg). The film oil pattern highlights the formation of a separation line on the fuselage surface in proximity of the tail leading edge, which is linked to the onset of a horseshoe vortex. The vortex structure bends around the tail leading edge and flows alongside the tail root, leading to corner flow separation downstream. Moreover, the oil pattern on the vertical tail shows that the shear lines curve outboard toward the trailing edge. This is probably due to the onset of crossflow caused by the streamlines curvature typical of swept wings.

Figure A3 reports the total pressure distribution at the trailing edge of the fuselage of the BF configuration in cruise conditions. The fuselage boundary layer presents a distribution which is largely axisymmetric. The wakes of the VTP and of the fuselage-support strut are clearly visible on the top and bottom sectors, respectively. At this location, the fuselage boundary-layer edge is equal to approximately $r/R_b = 0.7$.

Acknowledgments

This work was conducted within the CENTRELINe project, which has received funding from the European Union's Horizon 2020 research and innovation programme under Grant Agreement Number 723242. The authors wish to express their gratitude to Nando van Arnhem, Daniele Ragni, Tomas Sinnige, Reynard de Vries, and Sumit Tambe for their contribution to the design, execution, and analysis of the wind-tunnel experiments.

References

- [1] Wislicenus, G., "Hydrodynamics and Propulsion of Submerged Bodies," *ARS Journal*, Vol. 30, No. 12, 1960, pp. 1140–1148. <https://doi.org/10.2514/8.5351>
- [2] Gearhart, W., and Henderson, R., "Selection of a Propulsor for a Submersible System," *Journal of Aircraft*, Vol. 3, No. 1, 1966, pp. 84–90. <https://doi.org/10.2514/3.59270>
- [3] Smith, L. H., "Wake Ingestion Propulsion Benefit," *Journal of Propulsion and Power*, Vol. 9, No. 1, 1993, pp. 74–82. <https://doi.org/10.2514/3.11487>
- [4] Drela, M., "Power Balance in Aerodynamic Flows," *AIAA Journal*, Vol. 47, No. 7, 2009, pp. 1761–1771. <https://doi.org/10.2514/1.42409>
- [5] Lv, P., Gangoli Rao, A., Ragni, D., and Veldhuis, L., "Performance Analysis of Wake and Boundary-Layer Ingestion for Aircraft Design," *Journal of Aircraft*, Vol. 53, No. 5, 2016, pp. 1517–1526. <https://doi.org/10.2514/1.C03395>
- [6] Arntz, A., Atinault, O., and Merlen, A., "Exergy-Based Formulation for Aircraft Aeropropulsive Performance Assessment: Theoretical Develop-

- opment," *AIAA Journal*, Vol. 53, No. 6, 2015, pp. 1627–1639.
<https://doi.org/10.2514/1.J053467>
- [7] Arntz, A., and Atinault, O., "Exergy-Based Performance Assessment of a Blended Wing–Body with Boundary-Layer Ingestion," *AIAA Journal*, Vol. 53, No. 12, 2015, pp. 3766–3776.
<https://doi.org/10.2514/1.J054072>
- [8] Uranga, A., Drela, M., Greitzer, E. M., Hall, D. K., Titchener, N. A., Lieu, M. K., Siu, N. M., Casses, C., Huang, A. C., Gatlin, G. M., et al., "Boundary Layer Ingestion Benefit of the D8 Transport Aircraft," *AIAA Journal*, Vol. 55, No. 11, 2017, pp. 1–17.
- [9] Wiart, L., Atinault, O., Boniface, J.-C., and Barrier, R., "Aeropropulsive Performance Analysis of the NOVA Configurations," *30th Congress of the International Council of the Aeronautical Sciences*, 2016.
- [10] Wiart, L., and Negulescu, C., "Exploration of the Airbus 'Nautilus' Engine Integration Concept," *31st Congress of the International Council of the Aeronautical Sciences*, 2018.
- [11] Blumenthal, B. T., Elmiligui, A. A., Geiselhart, K. A., Campbell, R. L., Maughmer, M. D., and Schmitz, S., "Computational Investigation of a Boundary-Layer-Ingestion Propulsion System," *Journal of Aircraft*, Vol. 55, No. 3, 2018, pp. 1141–1153.
<https://doi.org/10.2514/1.C034454>
- [12] Steiner, H.-J., Seitz, A., Wieczorek, K., Plötner, K., Isikveren, A. T., and Hornung, M., "Multi-Disciplinary Design and Feasibility Study of Distributed Propulsion Systems," *28th International Congress of the Aeronautical Sciences*, 2012, pp. 23–28.
- [13] Welstead, J., and Felder, J. L., "Conceptual Design of a Single-Aisle Turboelectric Commercial Transport with Fuselage Boundary Layer Ingestion," *54th AIAA Aerospace Sciences Meeting*, AIAA Paper 2016-1027, 2016.
<https://doi.org/10.2514/6.2016-1027>
- [14] Seitz, A., Habermann, A. L., Peter, F., Troeltsch, F., Castillo Pardo, A., Della Corte, B., van Sluis, M., Goraj, Z., Kowalski, M., Zhao, X., Grönstedt, T., Bijewitz, J., and Wortmann, G., "Proof of Concept Study for Fuselage Boundary Layer Ingesting Propulsion," *Aerospace*, Vol. 8, No. 1, 2021, pp. 1–16.
<https://doi.org/10.3390/aerospace8010016>
- [15] Isikveren, A. T., Seitz, A., Bijewitz, J., Mirzoyan, A., Isyanov, A., Grenon, R., Atinault, O., Godard, J. L., and Stückl, S., "Distributed Propulsion and Ultra-High By-Pass Rotor Study at Aircraft Level," *Aeronautical Journal*, Vol. 119, No. 1221, 2015, pp. 1327–1376.
<https://doi.org/10.1017/S0001924000011295>
- [16] Castillo Pardo, A., and Hall, C. A., "Aerodynamics of Boundary Layer Ingesting Fuselage Fans," *Journal of Turbomachinery*, Vol. 143, No. 4, 2021, pp. 1–9.
<https://doi.org/10.1115/1.4049918>
- [17] Lv, P., Ragni, D., Hartuc, T., Veldhuis, L., and Gangoli Rao, A., "Experimental Investigation of the Flow Mechanisms Associated with a Wake-Ingesting Propulsor," *AIAA Journal*, Vol. 55, No. 4, 2016, pp. 1332–1342.
<https://doi.org/10.2514/1.J055292>
- [18] Atinault, O., Carrier, G., Grenon, R., Verbecke, C., and Viscat, P., "Numerical and Experimental Aerodynamic Investigations of Boundary Layer Ingestion for Improving Propulsion Efficiency of Future Air Transport," *31st AIAA Applied Aerodynamics Conference*, AIAA Paper 2013-2406, 2013, pp. 1–13.
<https://doi.org/10.2514/6.2013-2406>
- [19] Gray, J. S., Mader, C. A., Kenway, G. K., and Martins, J. R., "Modeling Boundary Layer Ingestion Using a Coupled Aeropropulsive Analysis," *Journal of Aircraft*, Vol. 55, No. 3, 2018, pp. 1191–1199.
<https://doi.org/10.2514/1.C034601>
- [20] Gray, J. S., Mader, C. A., Kenway, G. K., and Martins, J. R., "Coupled Aeropropulsive Optimization of a Three-Dimensional Boundary-Layer Ingestion Propulsor Considering Inlet Distortion," *Journal of Aircraft*, Vol. 57, No. 6, 2020, pp. 1014–1025.
<https://doi.org/10.2514/1.C035845>
- [21] Seitz, A., Habermann, A. L., and van Sluis, M., "Optimality Considerations for Propulsive Fuselage Power Savings," *Journal of Aerospace Engineering*, Vol. 235, No. 1, 2020, pp. 22–39.
<https://doi.org/10.1177/0954410020916319>
- [22] Della Corte, B., van Sluis, M., Gangoli Rao, A., and Veldhuis, L., "Power Balance Analysis Experiments on an Axisymmetric Fuselage with an Integrated Boundary-Layer-Ingesting Fan," *AIAA Journal*, Vol. 59, No. 12, 2021, pp. 5211–5244.
<https://doi.org/10.2514/1.J060570>
- [23] Gunn, E. J., and Hall, C. A., "Non-Axisymmetric Stator Design for Boundary Layer Ingesting Fans," *ASME Turbo Expo*, ASME Paper GT2017-63082, 2017.
<https://doi.org/10.1115/GT2017-63082>
- [24] Hall, D. K., Greitzer, E. M., and Tan, C. S., "Analysis of Fan Stage Design Attributes for Boundary Layer Ingestion," *ASME Turbo Expo*, ASME Paper GT2016-57808, 2016.
<https://doi.org/10.1115/GT2016-57808>
- [25] Mårtensson, H., "Harmonic Forcing from Distortion in a Boundary Layer Ingesting Fan," *Aerospace*, Vol. 8, No. 3, 2021, pp. 1–13.
<https://doi.org/10.3390/aerospace8030058>
- [26] Petrosino, F., Barbarino, M., and Staggat, M., "Aeroacoustics Assessment of an Hybrid Aircraft Configuration with Rear-Mounted Boundary Layer Ingested Engine," *Applied Sciences*, Vol. 11, No. 7, 2021.
<https://doi.org/10.3390/app11072936>
- [27] Romani, G., Ye, Q., Avallone, F., Ragni, D., and Casalino, D., "Numerical Analysis of Fan Noise for the NOVA Boundary-Layer Ingestion Configuration," *Aerospace Science and Technology*, Vol. 96, Jan. 2020.
<https://doi.org/10.1016/j.ast.2019.105532>
- [28] "A Method for Estimating Drag-Rise Mach Number at Zero Incidence of Smooth or Bumpy Non-Ducted Axisymmetric Bodies Without or With Fins," 74013, IHS ESDU, 1974.
- [29] Drew, B., and Jenn, A., "Pressure Drag Calculations on Axisymmetric Bodies of Arbitrary Moldline," *28th Aerospace Sciences Meeting*, AIAA Paper 1990-0280, 1990.
<https://doi.org/10.2514/6.1990-280>
- [30] Purvis, J. W., and Burkhalter, J. E., "Prediction of Critical Mach Number for Store Configurations," *AIAA Journal*, Vol. 17, No. 11, 1979, pp. 1170–1177.
<https://doi.org/10.2514/3.7617>
- [31] van Sluis, M., Della Corte, B., and Gangoli Rao, A., Final PFC Aircraft Aerodynamic Design and Analysis, CENTRELINe Public Deliverable D3.03, 2021.
- [32] Della Corte, B., van Sluis, M., and Gangoli Rao, A., Results of Overall Configuration Wind Tunnel Testing, CENTRELINe Public Deliverable D3.02, 2021.
- [33] Wieneke, B., "PIV Uncertainty Quantification from Correlation Statistics," *Measurement Science and Technology*, Vol. 26, No. 7, 2015, Paper 074002.
<https://doi.org/10.1088/0957-0233/26/7/074002>
- [34] Serpieri, J., "Cross-Flow Instability: Flow diagnostics and Control of Swept Wing Boundary Layers," Ph.D. Dissertation, Delft Univ. of Technology, Delft, The Netherlands, 2018.
- [35] Della Corte, B., Perpignan, A. A., van Sluis, M., and Gangoli Rao, A., "Experimental and Computational Analysis of Model-Support Interference in Low-Speed Wind-Tunnel Testing of Fuselage-Boundary-Layer Ingestion," *9th EASN Conference*, Vol. 304, Dec. 2019.
<https://doi.org/10.1051/matecconf/201930402020>
- [36] Cheskakas, C. J., Taylor, D., and Simpson, R. L., "Detailed Investigation of the Three-Dimensional Separation About a 6:1 Prolate Spheroid," *AIAA Journal*, Vol. 35, No. 6, 1997, pp. 990–999.
<https://doi.org/10.2514/2.208>
- [37] Bissinger, N. C., and Breuer, T., *Basic Principles—Gas Turbine Compatibility—Intake Aerodynamic Aspects*, Wiley, Hoboken, NJ, 2010.
<https://doi.org/10.1002/9780470686652.eae487>
- [38] Drela, M., "XFOIL: An Analysis and Design System for Low Reynolds Number Airfoils," *Low Reynolds Number Aerodynamics*, edited by T. J. Mueller, Springer-Verlag, New York, 1989, pp. 1–12.